AIP/123-QED

Non-equilibrium polyatomic gas flows: Nonlinear coupled constitutive relations and topological study of three-temperature relaxation

H. Srivastava (हर्षल श्रीवास्तव),[1] Tapan K. Mankodi (तपन के मंकोड़ी,),[1] and R. S. Myong (명노신)[2]

[1)]*Department of Mechanical Engineering, Indian Institute of Technology Guwahati, Guwahati, Assam 781039, India*

[2)]*School of Mechanical and Aerospace Engineering, and ACTRC, Gyeongsang National University, Jinju, Gyeongnam 52828, South Korea*

(*Electronic mail: myong@gnu.ac.kr)

Non-equilibrium gaseous phenomena at high temperatures may activate additional degrees of freedom that remain dormant at lower temperatures, such as vibrational modes. An accurate prediction of the forces and heat flux acting on a body in such an environment requires detailed information on the energy distribution among rotational and vibrational degrees of freedom. The present study aims to analyze non-equilibrium flows by carefully accounting for the relaxation processes among various degrees of freedom. As higher-order constitutive equations, the nonlinear coupled constitutive relations (NCCR) were employed to obtain more accurate approximations of the stress and heat flux terms by extending the two-temperature formulation proposed by Srivastava et al. [Phys. Fluids 37, 036154 (2025)] to a three-temperature relaxation case. The present study further examined various relaxation models for internal energy to evaluate their effectiveness and accuracy. In addition to the standard energy exchange that considers only translational and other modes, the energy exchange between rotational and vibrational degrees of freedom was investigated. A topological study was further incorporated to observe the changes in the solution space within the second-order NCCR formulation relative to the first-order constitutive relations, i.e., the Navier-Stokes-Fourier (NSF) formulation. Finally, the new set of equations derived from the three-temperature relaxation model was used to investigate shock wave structures in polyatomic gases.

I. INTRODUCTION

As interest in interplanetary flights has grown, concerns have also increased about the efficient maneuvering of spacecraft and protection from heat loads, which have become ever more challenging. Different flow regimes and high non-equilibrium conditions are involved, which have made the analysis of internal degrees of freedom increasingly important. Such high-temperature, rarefied, non-equilibrium environments are conducive to the excitation of several internal degrees of freedom and even chemical reactions, which remain dormant under ordinary conditions. These thermochemical effects alter surface properties, influencing the interaction between shock waves and the boundary layer, and thereby modifying aerothermodynamic loads, including surface pressure and heat transfer[1]. At very high temperatures, the surrounding gas may ionize, forming plasma that can attenuate radio signals, disrupt communication between the spacecraft and ground stations, and pose risks to safe landing[2,3].

The effect of internal degrees of freedom was initially attributed to the anomalous absorption of sound waves in gases[4]. Before that, the absorption of sound in gases was primarily attributed to the effects of viscous dissipation and thermal conduction[5] only. Later, experiments were devised to observe the dispersion of sound in air and carbon dioxide[6]. An initial attempt to explain the anomalous absorption was made by Herzfeld *et al.*[7]. He attributed observations to the energy exchange between the translational and internal degrees of freedom. Kneser[8] also concluded that the phenomenon of sound absorption in air and oxygen is due to the exchange of energy between the translational mode and the vibrational mode of oxygen.

The quantitative analysis of this exchange began with the analysis of Landau *et al.*[9]. Based on preliminary assumptions, they derived an equation describing vibrational relaxation in gases. This equation was used to relate the relaxation of the vibrational degree to the finite time required to reach equilibrium. Since the vibrational degree was observed to take a longer time to relax as compared to the translational and rotational degrees, most of the initial studies were linked with the vibrational relaxation, assuming the translational and rotational degrees to be in equilibrium with each other (Table I). In a report by Bethe *et al.*[10], the deviations from the equilibrium due to the presence of various degrees of freedom were analyzed. The degrees of freedom were divided into two groups based on their relaxation time: active and inert. The active group consisted of translational and rotational modes, whereas the inert group consisted of vibrational and dissociation modes. The temperature was based on the active degrees of freedom. Schwartz *et al.*[11] calculated

the vibrational relaxation time for gases using different temperatures to account for the energy in various degrees of freedom. They provided the formulation for calculating the relaxation times in pure gases, mixtures, and polyatomic gases.

The process to equilibrium is a complex phenomenon, and it is difficult to determine the amount of energy in a particular degree of freedom. The statistical formula relating temperatures to Boltzmann distributions is valid under equilibrium conditions. Often, equilibrium relations are extended to non-equilibrium conditions to obtain a transient temperature in a non-equilibrium relaxation mode. Studies by Rubin *et al.*[12] showed that, if Landau-Teller transition probabilities are used, an initial Boltzmann distribution retains its form throughout the relaxation process with a time-dependent temperature. However, the use of a different set of transition probabilities will not maintain the Boltzmann distribution throughout the relaxation process[13].

Further, Montroll *et al.*[24] included the phenomenon of radiative relaxation besides the collisional relaxation. They observed that, under the assumption of Landau-Teller transition probabilities, the initial Boltzmann distribution remained a Boltzmann distribution throughout the relaxation process. Herman *et al.*[25] included the relaxation of the rotational mode besides the vibrational mode. Transition probabilities between the translational and rotational degrees of freedom were calculated using those of Takayanagi[26]. The initial rotational-vibrational Boltzmann distribution was theoretically found to relax via a sequence of intermediate rotational and vibrational Boltzmann distributions.

Table I summarizes some of the experiments that have been performed to estimate the vibrational relaxation under different conditions using various techniques. Millikan *et al.*[27] obtained a curve-fit formula for the vibrational relaxation by considering most of the available experimental data. They observed that the relationship between $\log(p\tau_v)$ and $T^{-1/3}$ is a linear one and, for most of the systems, converges to a point near $p\tau_v = 10^{-8}$atm sec and $(T\ \mathrm{K})^{-1/3} = 0.03$. The approach provided good approximations for most cases, with a few exceptions that involved light colliding partners. It should be noted that Millikan *et al.* considered only translational to vibrational energy transfers and ignored the energy available in the rotational degree of the colliding partner.

Appleton[28] used the vacuum-ultraviolet light-absorption technique at 1176 Å for a shock tube study of nitrogen gas over the temperature range of 3000 to 9000 K. They validated the assumption that the vibrational levels relax via a sequence of "Boltzmann distributions" described by a single temperature. Later, Rich *et al.*[29] provided an analysis where such a sequence was not bound to be observed.

TABLE I: Determination of vibrational relaxation times

Author	Summary
Blackman[14]	An interferometric technique was employed to analyze vibrational relaxation in oxygen and nitrogen gases over the Mach number range of 3–10.
Sette *et al.*[15]	Ultrasonic velocity measurements were performed for CH_4, CH_3Cl, CH_2Cl_2, and CCl_4 to account for the dispersion of velocity in each case.
Miyahara *et al.*[16]	Relaxation in Freons was studied by measuring the wavelength and absorption coefficient of ultrasonic compressional waves.
Edmonds *et al.*[17]	The vibrational relaxation time in polyatomic gases was determined from measurements of acoustic absorption coefficients.
Shields[18]	Sound absorption due to vibrational relaxation was investigated using the tube method in halogen gases.
Dickens *et al.*[19]	New calculations of the vibrational relaxation times for acetylene, water, carbon monoxide, and iodine were presented following Tanczos[20].
Camac[21]	Vibrational and dissociation rates in O_2 were determined using the ultraviolet light absorption technique.
Matthews[22]	Vibrational relaxation in suddenly heated carbon monoxide was investigated using a shock tube and an interferometer over the temperature range of 2200-4900 K.
Parker[23]	The influence of O_2, D_2, and He on the vibrational relaxation time of O_2 in $O_2 - H_2, O_2 - D_2$, and $O_2 - He$ mixtures was investigated using an acoustic resonance tube.

Park[30] assessed a theoretical approach that involved two-temperature (TT_v) modeling of weakly ionizing and dissociating nitrogen gas with the available experimental data[31,32,33]. The translational equilibrium was assumed, and the temperature was taken to be equal to the heavy-particle translational temperature. The vibrational temperature of all molecules in all electronic states was assumed to be equal to the translational temperature of the electrons. Park pointed out the breakdown of the relaxation time expression of Millikan *et al.*[27] at higher temperatures.

Talbot[34], however, pointed out that assuming the equilibration of the translational and rotational degrees of freedom might not be justified in some cases. In fact, the experiments by Levitt *et al.*[35] proved that in the case of oxygen, the rotational relaxation was slower at higher temperatures. However, most later studies still focused on improving vibrational relaxation models and on their dependence on chemical reactions. The rotational non-equilibrium came into focus again when Sharma *et al.*[36] re-performed the AVCO's experiments[31,32,33] with better equipment. They observed that the rotational temperature obtained was considerably lower than that predicted by Park[30] and expected from the extrapolation of AVCO's experimental data.

Furudate *et al.*[37,38] conducted a ballistic range experiment over a sphere and a sharp cone in an intermediate hypersonic flow regime to investigate the two-temperature thermochemical model. The shock standoff distance was taken as a parameter for the investigation. The calculated shock layer thickness was thinner than the experimental data, where the flow field is chemically frozen and vibrationally highly excited. The introduction of multiple vibrational temperatures and rotational non-equilibrium significantly improved agreement between calculations and experiments[39]. Fujita *et al.*[40] reproduced the environmental conditions of re-entry vehicles such as the MUSES-C re-entry capsule, where the velocity is above 10 km/s in shock tubes. A significant difference was observed between the translational, rotational, and vibrational temperatures.

The rotational collision number calculated using Parker's[41] formulation provides an effective collision number on the order of 10. However, experiments conducted under certain conditions showed that the rotational degree takes a significant time to reach equilibrium values. Park[42] extrapolated the state-to-state transition-rate coefficient for N_2 proposed by Rahn *et al.*[43] to extremely high temperatures up to $128,000$ K to determine the effective collision number and characteristic relaxation times. He provided the expressions for energy transfer between rotational and vibrational modes. The proposed model was compared with the experimental results[40,36]. A satisfactory match was observed for vibrational and rotational temperatures. Park[44] also reviewed the limitations of the two-temperature model and even the need for more appropriate hydrodynamic equations, as Navier-Stokes-Fourier equations lose their validity at a high degree of equilibrium.

Recent studies have shifted towards the use of high-fidelity models that calculate relaxation phenomena directly using state-resolved equations. Boyd *et al.*[45] combined state-resolved models for vibrational excitation with DSMC simulations. To study the non-equilibrium flow fields in the hydrogen-based environments of Jovian planets, state-resolved models were developed by Kim *et al.*[46,47,48]. As the temperatures involved in the analysis increase, more degrees of freedom and

corresponding non-equilibrium temperatures were needed[49,50].

The present study employed second-order-accurate formulations and the nonlinear coupled constitutive relations (NCCR) developed by Myong[51]. NCCR is based on the generalized hydrodynamics (GH) approach of Eu[52]. Previously, the NCCR formulation was applied to studies related to hypersonic flow. Mankodi *et al.*[53] extended the NCCR formulation to vibrational relaxation.

The vibrational mode and chemical reactions are usually assumed to be in non-equilibrium with the translational and rotational modes[54,55]. The two-temperature approach was employed, and the energy exchange between the translational–rotational and vibrational modes was modeled using the Landau–Teller formulation. Recently, Srivastava *et al.*[56] addressed rotational non-equilibrium using a two-temperature model of the NCCR formulation. They, however, did not consider the effect of the vibrational degree of freedom. The multi-temperature NCCR formulation yielded better results than the NSF multi-temperature formulation. Also, the formulation was better than the single-temperature formulation, particularly at higher Mach numbers.

Zeng *et al.*[57] applied Park's two-temperature model with chemical models provided by Gupta *et al.*[58] to study a two-dimensional cylinder, the RAM-C II flight vehicle, and an HTV-2 flight vehicle in the NCCR framework. The results obtained were in better agreement with the DSMC simulations than with the NSF formulation results. Later, the model was extended to include thermochemical non-equilibrium effects[59]. Two separate formulations of the NCCR equations were solved: one with the evolution equation of the nonlinear vibrational heat flux and another with linear vibrational heat flux constitutive relations, similar to those in the NSF equations. The nonlinear model provided considerable improvement, producing more physically consistent results.

Recently, a data-driven three-temperature model was developed to yield results comparable to those of the DSMC simulations at lower cost. A deep neural network (DNN) model was trained on the DSMC data to learn the constitutive relations. The model mapped higher-order non-conserved moments using a first-order approximation, which was then integrated with the finite-volume method for solving the conservation laws[60,61].

The present study investigated the role of higher-order hydrodynamic equations in the three-temperature framework for hypersonic flows. This work is a continuation of our previous work[56], which involved two temperatures and accounted only for translational and rotational degrees of freedom. Since the vibrational mode becomes important as the flow temperature exceeds the gas's characteristic vibrational temperature, this study presents a new set of equations that explicitly account for it. A comparison was performed between the NSF, NCCR, and DSMC approaches, where

the present NCCR formulation was found to be more closely aligned with the DSMC results. The relaxation equations for rotational and vibrational degrees of freedom employed modified Landau–Teller equations as suggested by Park[42]. The vibrational relaxation time was evaluated using the Millikan–White equation[27] with Park's correction[42] for high temperatures. Several models can be used to calculate the rotational relaxation time[62,63,64,65]. However, a simplified approach was followed in this study, and the rotational relaxation time was calculated using Parker's model[41] and Park's model[42]. A comparative study between the two models is also presented.

The paper is organized into the following sections. Section II introduces the new set of equations that were solved to obtain the results. The nonlinear and coupled nature of the non-conserved moments in the second-order relations is highlighted through the non-dimensional form of the new set of equations. Section III provides a visual representation of the nature of the second-order moments, such as the stress tensor and various heat fluxes, as functions of first-order approximations through topological analysis. Section IV discusses the results related to the shock-structure simulation and the computational schemes used for this analysis. It also includes a detailed discussion of the various cases examined in the study, covering different types of relaxation mechanisms and models. Section V concludes the study by summarizing the major outcomes and proposing future extensions of the present work.

II. GOVERNING EQUATIONS

The fundamental equations for the conservation of mass, momentum, and total energy, along with equations accounting for the conservation of energy in each internal mode, form the central set of governing equations. The energy equation for each mode contains a corresponding source term (S_i), which accounts for the transfer of energy between different modes. The set of partial differential equations for the conserved variables, along with the energy equations for the rotational and vibrational degrees of freedom, is given as follows:

$$\begin{aligned}
\frac{\partial \rho}{\partial t} + \boldsymbol{\nabla}\cdot(\rho \boldsymbol{u}) &= 0 \\
\frac{\partial}{\partial t}(\rho \boldsymbol{u}) + \boldsymbol{\nabla}\cdot(p\boldsymbol{I} + \rho \boldsymbol{u}\boldsymbol{u}) + \boldsymbol{\nabla}\cdot\boldsymbol{\Pi} &= 0 \\
\frac{\partial}{\partial t}(\rho E) + \boldsymbol{\nabla}\cdot\{(\rho E + p)\boldsymbol{u}\} + \boldsymbol{\nabla}\cdot(\boldsymbol{\Pi}\cdot\boldsymbol{u} + \boldsymbol{Q}) &= 0 \\
\frac{\partial}{\partial t}(\rho E_{i(=r/v)}) + \boldsymbol{\nabla}\cdot\{(\rho E_{i(=r/v)})\boldsymbol{u}\} + \boldsymbol{\nabla}\cdot\boldsymbol{Q}_{i(=r/v)} &= S_{i(=r/v)}
\end{aligned} \tag{1}$$

where ρ is the density, t is the time variable, $\boldsymbol{u}$ is the bulk velocity, p is the pressure, $\boldsymbol{\Pi}$ is the stress tensor, E is the total energy per unit mass ($= E_t + E_r + E_v + u^2/2$) which is the sum of translational (E_t), rotational (E_r), vibrational (E_v) energies per unit mass, and the per unit mass bulk kinetic energy ($u^2/2$), $\boldsymbol{Q}$ is the total heat flux ($= \boldsymbol{Q}_t + \boldsymbol{Q}_r + \boldsymbol{Q}_v$) which is the sum of translational ($\boldsymbol{Q}_t$), rotational ($\boldsymbol{Q}_r$), and vibrational ($\boldsymbol{Q}_v$) heat fluxes, S_r is the source term for rotational-translational energy transfer, and S_v is the source term for vibrational-translational energy transfer. Eq. (1) also forms the basis of the DNN study by Garg *et al.*[61]. The ideal gas equation of state is given below.

$$p = \rho R T_t \tag{2}$$

where R is the gas constant and T_t is the translational temperature. The expressions for the energy densities of different modes per unit mass are given below.

$$E_t = \frac{3}{2} R T_t, \quad E_r = R T_r, \quad E_v = \frac{R\theta_v}{e^{(\theta_v/T_v)} - 1}, \tag{3}$$

where T_r is the rotational temperature, T_v is the vibrational temperature, and θ_v is the characteristic vibrational temperature. The source terms are modeled using the modified Landau-Teller expressions[42], which account for the rotational-vibrational energy transfer.

$$S_r = \rho \left\{ \frac{E_r(T_t) - E_r}{\tau_r} + 0.4 \frac{E_v - E_v(T_r)}{\tau_{MW}} \right\} \tag{4}$$

$$S_v = \rho \left\{ 0.6 \frac{E_v(T_t) - E_v}{\tau_{MW} + \tau_P} + 0.4 \frac{E_v(T_r) - E_v}{\tau_{MW}} \right\} \tag{5}$$

where $E_r(T_t)$ is its equilibrium rotational energy density value at the translational temperature, while E_r is the instantaneous value of the rotational energy density. $E_v(T_t)$ is the equilibrium vibrational energy density value corresponding to the translational temperature (T_t), E_v is the instantaneous value of vibrational energy density, and $E_v(T_r)$ is the equilibrium vibrational energy density value at the rotational temperature (T_r). The term τ_r is the rotational relaxation time, τ_{MW} is the vibrational relaxation time as per the Millikan-White (MW) model, and τ_P is Park's correction to the relaxation time predicted by the Millikan-White model. The last term in the L.H.S. of Eq. (4) accounts for the energy exchange between the rotational and vibrational modes.

The rotational relaxation time can be handled using either Parker's[41] or Park's model[42]. In Parker's model, the rotational relaxation time is given as:

$$\tau_r = Z_r \tau_c \tag{6}$$

where $\tau_c = (\pi/4)(\eta/p)$ is the mean collision time and (Z_r) is the mean collision number, which is a function of only the translational temperature and has the following form:

$$Z_r(T_t) = \frac{Z_r^{\infty}}{\left\{1 + \frac{\pi^{\frac{3}{2}}}{2}\left(\frac{T'}{T_t}\right)^{\frac{1}{2}} + \left(2 + \frac{\pi^2}{4}\right)\left(\frac{T'}{T_t}\right)\right\}} \tag{7}$$

where T' and Z_r^{∞} are gas specific parameters. The formula in Eq. (7) is the corrected one after considering the Brau *et al.*[66] correction. In the first set of shock structure simulations in this work, constant values of Z_r and Z_v are used to calculate the relaxation times for the rotational and vibrational modes, without accounting for energy exchange between them. The corresponding Landau-Teller equations simplify to the following:

$$S_v = \rho\left(\frac{E_v(T_t) - E_v}{\tau_v}\right), \quad S_r = \rho\left(\frac{E_r(T_t) - E_r}{\tau_r}\right) \tag{8}$$

where $\tau_v (= Z_v \tau_c)$ was evaluated using a similar formula as given in Eq. (6). However, it is worth noting that temperature-dependent rotational and vibrational relaxation models are better suited to realistic simulations. Park[42] noted that Parker's formula for the rotational relaxation time was tested for temperatures less than 1500 K, and its accuracy is compromised at higher temperatures. Using an extrapolation of the expression provided by Rahn et al[43], he proposed the following fit for the rotational relaxation time:

$$p\tau_r = 2.46 \times 10^{-14} T_t^{1.692} \quad (\text{atm} - \text{s}) \tag{9}$$

where pressure (p) is in atm. The vibrational relaxation time was calculated using the Millikan-White expression[27].

$$\ln(p\tau_{MW}) = (1.16 \times 10^{-3})\sqrt{\mu}\,\theta_v^{4/3}(T_t^{-1/3} - 0.015\mu^{1/4}) - 18.42 \tag{10}$$

where pressure (p) is in atm, characteristic vibrational temperature (θ_v) and translational temperature (T_t) are in K. The variable μ is the reduced mass of the colliding pair. The curve fit expression (Eq. (10)) is valid up to temperatures of 8000 K; and further, Park[67] included a correction (τ_P) for higher temperature applications. The total vibrational relaxation time τ_v after the application of such a correction is given below.

$$\tau_v = \tau_{MW} + \tau_P \tag{11}$$

The expression for τ_P is given below[67]:

$$\tau_P = \frac{1}{n\sigma\bar{C}}, \quad \bar{C} = \sqrt{\frac{8}{\pi}\frac{k_B T_t}{m}} \tag{12}$$

where n is the number density, σ is the effective cross-section and $\bar{C}$ is the average molecular velocity, k_B is the Boltzmann constant and m is the molecule mass in kg.

In the NSF formulation, the calculations of non-conserved moments such as $\boldsymbol{\Pi}$ and $\boldsymbol{Q}$ are carried out using Newton's law of viscosity and Fourier's law of heat conduction.

$$\boldsymbol{\Pi} = -2\eta[\boldsymbol{\nabla u}]^{(2)} \tag{13}$$

$$\boldsymbol{Q}_{t/r/v} = -k_{t/r/v}\boldsymbol{\nabla} T_{t/r/v} \tag{14}$$

where η is the coefficient of viscosity, symbol $[\ ]^{(2)}$ denotes the traceless symmetric part of a tensor $\left([\boldsymbol{\nabla u}]^{(2)} = \frac{1}{2}[\boldsymbol{\nabla u} + (\boldsymbol{\nabla u})^t] - \frac{1}{3}\boldsymbol{I}\boldsymbol{\nabla}\cdot\boldsymbol{u}\right)$, k_i is the thermal conductivity of i^{th} internal energy mode (translational/rotational/vibrational mode). Equations (13) and (14) predict the non-equilibrium behavior of the flow with sufficient accuracy if the degree of non-equilibrium is small. This occurs for most phenomena observed; however, in situations involving a high degree of non-equilibrium, such as hypersonic flows, it results in an inaccurate description of the phenomenon. The higher-order formulations, such as the NCCR, are more appropriate for such situations. NCCR is based on generalized hydrodynamics[52], which provides separate partial differential equations for the non-conserved moments in addition to the conservation laws. The general evolution equation for the non-conserved moments takes the following form:

$$\rho\frac{d}{dt}\hat{\Phi}^{(\alpha)} = Z^{(\alpha)} + \Lambda^{(\alpha)} \tag{15}$$

where $\hat{\Phi} = \Phi/\rho$ for the higher-order moment Φ, $Z^{(\alpha)}$ is the kinematic term and $\Lambda^{(\alpha)}$ is the dissipative term for the moment labeled by α $(= (1), (2)\cdots)$[52] . The evolution equation for stress $(\boldsymbol{\Pi})$ and translational heat flux $(\boldsymbol{Q}_t)$ can be obtained by substituting Φ with the expressions of $< m[\boldsymbol{cc}]^{(2)} f >$ and $< \frac{1}{2}mc^2\boldsymbol{c}f >$[52] with m and c as the mass and the peculiar velocity and f as the probability distribution function integrated $(<>)$ with respect to peculiar velocity. The set of equations obtained is given below:

$$\rho\frac{d\hat{\boldsymbol{\Pi}}}{dt} = -\boldsymbol{\nabla}\cdot\psi_1 - 2[\boldsymbol{\Pi}\cdot\boldsymbol{\nabla u}]^{(2)} - \frac{p}{\eta}\left\{\boldsymbol{\Pi}q(\kappa) + 2\eta[\boldsymbol{\nabla u}]^{(2)}\right\} \tag{16}$$

$$\begin{aligned}\rho\frac{d\hat{\boldsymbol{Q}}_t}{dt} &= -\boldsymbol{\nabla}\cdot\psi_3 + \left\{\boldsymbol{\nabla}\cdot(p\boldsymbol{I}+\boldsymbol{\Pi})\right\}\cdot\frac{\boldsymbol{\Pi}}{\rho} - \boldsymbol{Q}_t\cdot(\boldsymbol{\nabla u}) - \phi^{(3)} : (\boldsymbol{\nabla u}) \\ &\quad -C_{p,t}\boldsymbol{\Pi}\cdot\boldsymbol{\nabla} T_t - \frac{C_{p,t}p}{k_t}\left\{k_t T_t\boldsymbol{\nabla}(\ln T_t) + \boldsymbol{Q}_t q(\kappa)\right\}\end{aligned} \tag{17}$$

where ψ_1, ψ_3, and $\phi^{(3)}$ are the higher-order moments, and $C_{p,t}$ is the specific heat capacity at constant pressure for the translational mode. Traditionally, the excess stress was numbered as

the second non-conserved moment ($\Phi^{(2)}$) for studying diatomic gases using a single-temperature framework[68]. Since the present formulation employs a multi-temperature framework, the excess stress term is not needed[56]. However, the numbering for heat flux has not been altered to maintain consistency with the previous literature. The $q(\kappa)$ is a nonlinear function of κ which is analogous to the Rayleigh-Onsager dissipation function.

$$q(\kappa) = \frac{\sinh(\kappa)}{\kappa} \tag{18}$$

where κ for monoatomic gases is given as

$$\kappa = \frac{(mk_B)^{1/4}}{\sqrt{2}d}\frac{T_t^{1/4}}{p}\left[\frac{\boldsymbol{\Pi}:\boldsymbol{\Pi}}{2\eta} + \frac{\boldsymbol{Q}_t \cdot \boldsymbol{Q}_t/T_t}{k_t}\right]^{1/2} \tag{19}$$

Equations (16) and (17) need a closure to handle the higher-order moments (ψ_1, ψ_3 and $\phi^{(3)}$). Among closure theories, we employed the "closing-last balanced closure" as proposed by Myong[69]. Myong observed that there are two places to be closed (movement and interaction), rather than one (movement only). The order of approximations in handling the kinematic (movement) ψ and dissipation (interaction) $\Lambda^{(\alpha)}$ terms must be the same to satisfy balancing, for instance, the second-order closure for both terms. The present balanced closure effectively resolves the weakness of Eu's closure[70], where it was assumed that $\psi_i = 0$. This was challenged by mathematicians and physicists for its inconsistency, i.e., that the term ψ_i cannot be zero in general, especially in strong thermal non-equilibrium[71]. Instead, Myong assumed the following relations to be valid:

$$\boldsymbol{\nabla}\cdot\psi_1 = \boldsymbol{\nabla}\cdot\psi_3 + \phi^{(3)} : (\boldsymbol{\nabla}\boldsymbol{u}) = 0 \tag{20}$$

In this balanced closure theory, third-order closure for ψ_1 in the constitutive equation of the stress term may not be essential; in fact, the unbalanced higher-order closure in the moment method may not provide improved solutions as promised, especially in the case of a high Mach number shock structure problem.

Similar to the two-temperature framework[53], the non-equilibrium distribution function for the polyatomic gas flows is modified to include both the rotational and vibrational energy, which, upon derivation, leads to the evolution equations for rotational ($\boldsymbol{Q}_r$) and vibrational ($\boldsymbol{Q}_v$) heat fluxes required for the three-temperature framework. The rotational and vibrational heat flux equations have the following form, similar to Eq. (17):

$$\rho\frac{d\hat{\boldsymbol{Q}}_r}{dt} = -\boldsymbol{Q}_r\cdot(\boldsymbol{\nabla u}) - C_{p,r}\boldsymbol{\Pi}\cdot\boldsymbol{\nabla}T_r - \frac{C_{p,r}p}{k_r}\Big\{k_rT_r\boldsymbol{\nabla}(\ln T_r) + \boldsymbol{Q}_rq(\kappa)\Big\} \tag{21}$$

$$\rho\frac{d\hat{\boldsymbol{Q}}_v}{dt} = -\boldsymbol{Q}_v\cdot(\boldsymbol{\nabla u}) - C_{p,v}\boldsymbol{\Pi}\cdot\boldsymbol{\nabla}T_v - \frac{C_{p,v}p}{k_v}\Big\{k_vT_v\boldsymbol{\nabla}(\ln T_v) + \boldsymbol{Q}_vq(\kappa)\Big\} \tag{22}$$

The above evolution equations for the internal modes do not have the term $\{\boldsymbol{\nabla}\cdot(p\boldsymbol{I}+\boldsymbol{\Pi})\}\cdot(\boldsymbol{\Pi}/\rho)$ as present in Eq. (17) since these terms are related to the translational mode only. The κ is modified to include the terms corresponding to the rotational and vibrational modes, which takes the following form after employing the cumulant expansion:

$$\kappa = \frac{(mk_B)^{1/4}}{\sqrt{2}d}\frac{T_t^{1/4}}{p}\left[\frac{\boldsymbol{\Pi}:\boldsymbol{\Pi}}{2\eta} + \frac{\boldsymbol{Q}_t\cdot\boldsymbol{Q}_t/T_t}{k_t} + \frac{\boldsymbol{Q}_r\cdot\boldsymbol{Q}_r/T_r}{k_r} + \frac{\boldsymbol{Q}_v\cdot\boldsymbol{Q}_v/T_v}{k_v}\right]^{1/2} \tag{23}$$

The form of κ in the present set of equations is analogous to the Rayleigh-Onsager dissipation function derived for the monoatomic gas case.

A. Adiabatic approximation (NCCR Formulation)

Since the time scale at which non-conserved moments change is much smaller than the time scale at which macroscopic properties change, the non-conserved moments can be assumed to have reached a steady state without any perceptible change in the macroscopic properties involved in their calculation. This assumption simplifies the analysis by replacing the transient set of evolution equations with their steady-state counterparts[51]. Moreover, following Myong's NCCR formulation[51], the equations can be further simplified to the following set of equations:

$$-2[\boldsymbol{\Pi}\cdot\boldsymbol{\nabla u}]^{(2)} - \frac{p}{\eta}\Big\{\boldsymbol{\Pi}q(\kappa) + 2\eta[\boldsymbol{\nabla u}]^{(2)}\Big\} = 0 \tag{24}$$

$$-C_{p,t}\boldsymbol{\Pi}\cdot\boldsymbol{\nabla}T_t - \frac{C_{p,t}p}{k_t}\Big\{k_tT_t\boldsymbol{\nabla}(\ln T_t) + \boldsymbol{Q}_tq(\kappa)\Big\} = 0 \tag{25}$$

$$-C_{p,r}\boldsymbol{\Pi}\cdot\boldsymbol{\nabla}T_r - \frac{C_{p,r}p}{k_r}\Big\{k_rT_r\boldsymbol{\nabla}(\ln T_r) + \boldsymbol{Q}_rq(\kappa)\Big\} = 0 \tag{26}$$

$$-C_{p,v}\boldsymbol{\Pi}\cdot\boldsymbol{\nabla}T_v - \frac{C_{p,v}p}{k_v}\Big\{k_vT_v\boldsymbol{\nabla}(\ln T_v) + \boldsymbol{Q}_vq(\kappa)\Big\} = 0 \tag{27}$$

B. Non-dimensionalization

The multi-temperature NCCR relations were non-dimensionalized using the relations in Eq. (28) where ΔT represents the difference between the wall temperature and local temperature[51],

and L is the length scale.

$$\begin{aligned}
\boldsymbol{x}^* &= \frac{\boldsymbol{x}}{L}, & \eta^* &= \frac{\eta}{\eta_{ref}}, & \boldsymbol{u}^* &= \frac{\boldsymbol{u}}{u_{ref}}, \\
p^* &= \frac{p}{p_{ref}}, & \rho^* &= \frac{\rho}{\rho_{ref}}, & E^*_{(t/r/v)} &= \frac{E_{(t/r/v)}}{u^2_{ref}}, \\
T^*_{(t/r/v)} &= \frac{T_{(t/r/v)}}{T_{ref}}, & t^* &= \frac{t}{L/u_{ref}}, & k^*_{(t/r/v)} &= \frac{k_{(t/r/v)}}{k_{(t/r/v)ref}}, \\
C^*_{p,(t/r/v)} &= \frac{C_{p,(t/r/v)}}{C_{p,(t/r/v)ref}}, & \boldsymbol{\Pi}^* &= \frac{\boldsymbol{\Pi}}{\eta_{ref}u_{ref}/L}, & \boldsymbol{Q}^*_{(t/r/v)} &= \frac{\boldsymbol{Q}_{(t/r/v)}}{k_{(t/r/v)}\Delta T/L}
\end{aligned} \tag{28}$$

The conservation laws in their non-dimensional form are given below:

$$\frac{\partial \rho^*}{\partial t^*} + \boldsymbol{\nabla}^* \cdot (\rho^* \boldsymbol{u}^*) = 0 \tag{29}$$

$$\frac{\partial (\rho^* \boldsymbol{u}^*)}{\partial t^*} + \boldsymbol{\nabla}^* \cdot \left(\frac{1}{N_\delta Re} p^* \boldsymbol{I} + \rho^* \boldsymbol{u}^* \boldsymbol{u}^* \right) + \boldsymbol{\nabla}^* \cdot \left(\boldsymbol{\Pi}^* \frac{1}{Re} \right) = 0 \tag{30}$$

$$\begin{aligned}
&\frac{\partial (\rho^* E^*)}{\rho t^*} + \boldsymbol{\nabla}^* \cdot \left(\rho^* E^* + p^* \frac{1}{N_\delta Re} \right) \boldsymbol{u}^* \\
&+ \left(\frac{1}{Re} \right) \boldsymbol{\nabla}^* \cdot \left(\boldsymbol{\Pi}^* \cdot \boldsymbol{u}^* + \frac{\boldsymbol{Q}^*_t}{Ec_t Pr} + \frac{\boldsymbol{Q}^*_r}{Ec_r Pr} + \frac{\boldsymbol{Q}^*_v}{Ec_v Pr} \right) = 0
\end{aligned} \tag{31}$$

$$\frac{\partial (\rho^* E^*_r)}{\partial t^*} + \boldsymbol{\nabla}^* \cdot (\rho^* E^*_r) \boldsymbol{u}^* + \left(\frac{1}{Re} \right) \boldsymbol{\nabla}^* \cdot \left(\frac{\boldsymbol{Q}^*_r}{Ec_r Pr} \right) = S^*_r \tag{32}$$

$$\frac{\partial (\rho^* E^*_v)}{\partial t^*} + \boldsymbol{\nabla}^* \cdot (\rho^* E^*_v) \boldsymbol{u}^* + \left(\frac{1}{Re} \right) \boldsymbol{\nabla}^* \cdot \left(\frac{\boldsymbol{Q}^*_v}{Ec_v Pr} \right) = S^*_v \tag{33}$$

where $\boldsymbol{\nabla}^* = \partial / \partial \boldsymbol{x}^*$. The non-dimensional numbers such as the Reynolds number (Re), Prandtl number (Pr), Eckart number $(Ec_{(t/r/v)})$, Mach number (M), and $\boldsymbol{\nabla}^*$ are defined as:

$$\begin{aligned}
N_\delta &= \frac{\eta_{ref} u_{ref}}{p_{ref} L}, \quad Re = \frac{\rho_{ref} u_{ref} L}{\eta_{ref}}, \quad M = \frac{u_{ref}}{\sqrt{\gamma R T_{ref}}}, \\
Ec_{(t/r/v)} &= \frac{u^2_{ref}}{C_{p,(t/r/v)ref} \Delta T}, \quad Pr = \frac{C_{p,(t/r/v)ref} \eta_{ref}}{k_{(t/r/v)ref}}
\end{aligned} \tag{34}$$

If we assume the corresponding E_r and E_v in Eq. (8) being at the Boltzmann distribution at temperature T_r and T_v, the non-dimensionalized source terms can be written as below:

$$S^*_r = \frac{\rho^*}{\gamma M^2} \frac{(T^*_t - T^*_r)}{\tau^*_r}, \quad S^*_v = \frac{\rho^*}{\gamma M^2} \left(\frac{\theta^*_v}{e^{(\theta^*_v / T^*_t)} - 1} - \frac{\theta^*_v}{e^{(\theta^*_v / T^*_v)} - 1} \right) \Bigg/ \tau^*_v \tag{35}$$

The non-dimensional form of the stress tensor, translational, rotational, and vibrational fluxes are given below.

$$-2[\boldsymbol{\Pi}^*\cdot\boldsymbol{\nabla}^*\boldsymbol{u}^*]^{(2)}-\frac{1}{N_\delta}\frac{p^*}{\eta^*}\left\{\boldsymbol{\Pi}^* q(\kappa^* N_\delta)+2\eta^*[\boldsymbol{\nabla}^*\boldsymbol{u}^*]^{(2)}\right\}=0, \tag{36}$$

$$-Pr\boldsymbol{\Pi}^*\cdot\boldsymbol{\nabla}^* T_t^*-\frac{Pr}{N_\delta}\frac{p^*}{k_t^*}\left\{k_t^* T_t^*\boldsymbol{\nabla}^*(\ln T_t^*)+\boldsymbol{Q}_t^* q(N_\delta\kappa^*)\right\}=0, \tag{37}$$

$$-Pr\boldsymbol{\Pi}^*\cdot\boldsymbol{\nabla}^* T_r^*-\frac{Pr}{N_\delta}\frac{p^*}{k_r^*}\left\{k_r^* T_r^*\boldsymbol{\nabla}^*(\ln T_r^*)+\boldsymbol{Q}_r^* q(N_\delta\kappa^*)\right\}=0, \tag{38}$$

$$-Pr\boldsymbol{\Pi}^*\cdot\boldsymbol{\nabla}^* T_v^*-\frac{Pr}{N_\delta}\frac{p^*}{k_v^*}\left\{k_v^* T_v^*\boldsymbol{\nabla}^*(\ln T_v^*)+\boldsymbol{Q}_v^* q(N_\delta\kappa^*)\right\}=0 \tag{39}$$

The nonlinear non-dimensional κ is given below:

$$\kappa=N_\delta\kappa^*=\frac{cN_\delta}{p^*}\left[\boldsymbol{\Pi}^*:\boldsymbol{\Pi}^*+2\varepsilon_t\frac{\eta^*}{k_t^* T_t^*}\boldsymbol{Q}_t^*\cdot\boldsymbol{Q}_t^*+2\varepsilon_r\frac{\eta^*}{k_r^* T_r^*}\boldsymbol{Q}_r^*\cdot\boldsymbol{Q}_r^*+2\varepsilon_v\frac{\eta^*}{k_v^* T_v^*}\boldsymbol{Q}_v^*\cdot\boldsymbol{Q}_v^*\right] \tag{40}$$

where

$$c=\frac{1}{2}\left[8\frac{\sqrt{\pi}}{5}\Gamma\left(4-\frac{2}{\nu-1}\right)A_2(\nu)\right]^{1/2}\quad\text{and}\quad\varepsilon_{(t/r/v)}=\frac{1}{Ec_{(t/r/v)}Pr}\frac{1}{T_{ref}/\Delta T} \tag{41}$$

The value of $A_2(\nu)$ is tabulated in Srivastava *et al.*[56]. Equations (36)-(39) can be written as:

$$\hat{\boldsymbol{\Pi}}^* q(N_\delta\kappa^*) = \hat{\boldsymbol{\Pi}}_0^*+[\hat{\boldsymbol{\Pi}}^*\cdot\boldsymbol{\nabla}^*\hat{\boldsymbol{u}}^*]^{(2)}, \tag{42}$$

$$\hat{\boldsymbol{Q}}_t^* q(N_\delta\kappa^*) = \hat{\boldsymbol{Q}}_{t_0}^*+\hat{\boldsymbol{\Pi}}^*\cdot\hat{\boldsymbol{Q}}_{t_0}^*, \tag{43}$$

$$\hat{\boldsymbol{Q}}_r^* q(N_\delta\kappa^*) = \hat{\boldsymbol{Q}}_{r_0}^*+\hat{\boldsymbol{\Pi}}^*\cdot\hat{\boldsymbol{Q}}_{r_0}^*, \tag{44}$$

$$\hat{\boldsymbol{Q}}_v^* q(N_\delta\kappa^*) = \hat{\boldsymbol{Q}}_{v_0}^*+\hat{\boldsymbol{\Pi}}^*\cdot\hat{\boldsymbol{Q}}_{v_0}^*, \tag{45}$$

where $\boldsymbol{\Pi}_0^*,\boldsymbol{Q}_{t_0}^*,\boldsymbol{Q}_{r_0}^*$ and $\boldsymbol{Q}_{v_0}^*$ are the NSF fluxes converted to $\hat{\boldsymbol{\Pi}}_0^*,\hat{\boldsymbol{Q}}_{t_0}^*,\hat{\boldsymbol{Q}}_{r_0}^*$ and $\hat{\boldsymbol{Q}}_{v_0}^*$ using the following equations.

$$\boldsymbol{\nabla}^*\hat{\boldsymbol{u}}^*=-2N_\delta\frac{\eta^*}{p^*}\boldsymbol{\nabla}^*\boldsymbol{u}^*,\quad\hat{\boldsymbol{\Pi}}^*=\frac{N_\delta}{p^*}\boldsymbol{\Pi}^*, \tag{46}$$

$$\hat{\boldsymbol{Q}}_t^*=\frac{N_\delta}{p^*}\frac{\boldsymbol{Q}_t^*}{\sqrt{T_t^*/2\varepsilon_t}},\quad\hat{\boldsymbol{Q}}_r^*=\frac{N_\delta}{p^*}\frac{\boldsymbol{Q}_r^*}{\sqrt{T_r^*/2\varepsilon_r}},\quad\hat{\boldsymbol{Q}}_v^*=\frac{N_\delta}{p^*}\frac{\boldsymbol{Q}_v^*}{\sqrt{T_v^*/2\varepsilon_v}}, \tag{47}$$

and

$$\kappa=c\hat{R},\quad q(c\hat{R})=\frac{\sinh(c\hat{R})}{c\hat{R}}, \tag{48}$$

$$\hat{R}=\left(\hat{\boldsymbol{\Pi}}^*:\hat{\boldsymbol{\Pi}}^*+\hat{\boldsymbol{Q}}_t^*\cdot\hat{\boldsymbol{Q}}_t^*+\hat{\boldsymbol{Q}}_r^*\cdot\hat{\boldsymbol{Q}}_r^*+\hat{\boldsymbol{Q}}_v^*\cdot\hat{\boldsymbol{Q}}_v^*\right)^{1/2} \tag{49}$$

For the present study, we are interested in one-dimensional equations, which simplify the tensorial and vector equations to the following algebraic equations (The superscript $*$ is dropped for simplified representation):

$$\begin{aligned} \hat{\Pi} q(N_\delta \kappa) &= \hat{\Pi}_0 + \hat{\Pi}\hat{\Pi}\hat{\Pi}_0, \qquad & \hat{Q}_t q(N_\delta \kappa) &= \hat{Q}_{t_0} + \hat{\Pi}\hat{Q}_{t_0}, \\ \hat{Q}_r q(N_\delta \kappa) &= \hat{Q}_{r_0} + \hat{\Pi}\hat{Q}_{r_0}, \qquad & \hat{Q}_v q(N_\delta \kappa) &= \hat{Q}_{v_0} + \hat{\Pi}\hat{Q}_{v_0}. \end{aligned} \tag{50}$$

and

$$\hat{R} = \left(\frac{3}{2}\hat{\Pi}^2 + \hat{Q}_t^2 + \hat{Q}_r^2 + \hat{Q}_v^2 \right)^{1/2} \tag{51}$$

The set of Eqs. (50) - (51) represents a system of nonlinear algebraic equations. This is highlighted in Section III, which presents various sets of contour plots between various first and second-order non-conserved moments.

III. TOPOLOGICAL ANALYSIS

Topology is defined as the mathematical study of geometric properties that remain invariant under continuous deformations, such as stretching, twisting, and bending, without tearing or gluing. Formally, a topological space is characterized as an ordered pair comprising a set of points and a predefined collection of open sets. The investigation of topology has a long-standing history and remains a fundamental pillar in both mathematics and the physical sciences. For instance, the topological characteristics of conic sections are manifested in the trajectories of celestial bodies. These include the elliptical, parabolic, and hyperbolic orbits of planets and comets within our solar system, all of which are fundamentally governed by Kepler's laws of planetary motion.

Recently, a topological study conducted by Singh *et al.*[72] for velocity shear showed that the second-order NCCR constitutive model is governed by a conic section, which was expressed as a second-degree polynomial equation in the phase space. In addition, Garg *et al.*[73] investigated manifold structures and the kinematic constraints of viscous stresses and heat fluxes in velocity-shear flows by comparing DSMC data with NCCR theory. It was found that the mapping between the DSMC and NCCR moments identified the physical bounds and nonlinear correlations within the constitutive phase space, providing the necessary structural foundation for a deep neural network-based model[60,61] that accelerates finite-volume solutions for non-equilibrium gas dynamics.

A similar topological study was conducted in this work to demonstrate the nonlinear and coupled nature of the various second-order approximations of non-conserved moments. A four-dimensional

hypersurface for each of the non-conserved moments $\hat{\Pi}$, $\hat{Q}_t$, $\hat{Q}_r$ and $\hat{Q}_v$ as a function of their corresponding four first-order NSF approximations ($\hat{\Pi}_0$, $\hat{Q}_{t_0}$, $\hat{Q}_{r_0}$ and $\hat{Q}_{v_0}$) becomes difficult to visualize and necessitates the use of projections by keeping some of the quantities constant.

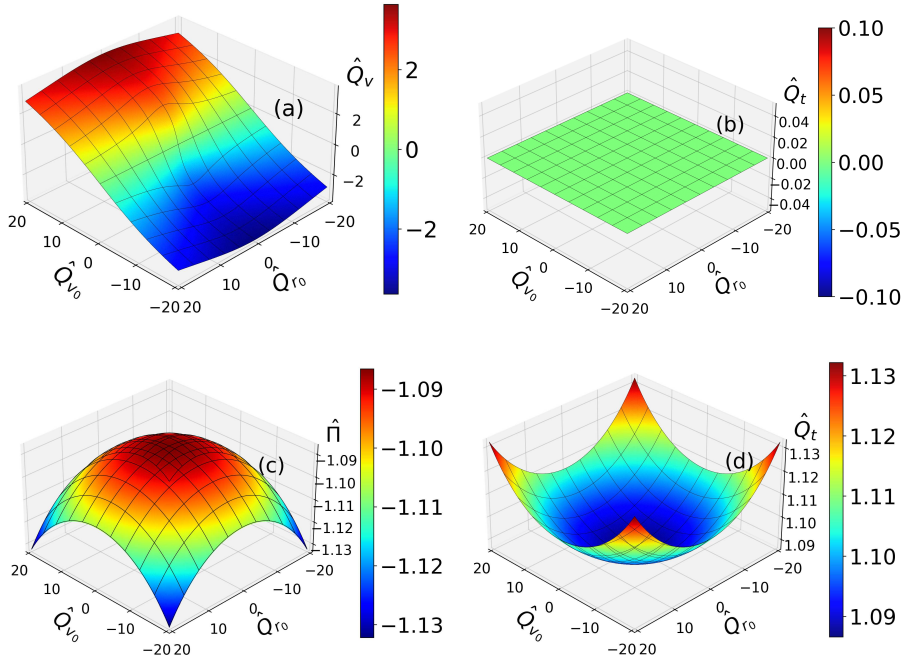

FIG. 1: Three-dimensional topologies of NCCR fluxes as a function of the constant values of NSF $\hat{\Pi}_0$ and NSF $\hat{Q}_{t_0}$, (a) Nonlinear positive correlation ($\hat{\Pi}_0 = 0, \hat{Q}_{t_0} = 0$), (b) Zero value ($\hat{\Pi}_0 = 20, \hat{Q}_{t_0} = 0$), (c) Symmetric maxima ($\hat{\Pi}_0 = 20, \hat{Q}_{t_0} = 20$), (d) Symmetric minima ($\hat{\Pi}_0 = 20, \hat{Q}_{t_0} = -20$).

The topological plots have been derived using Eqs. (50) and (51). The NSF terms in these equations were calculated using the velocity and temperature gradients obtained using the NCCR formulation. This is evident as $\boldsymbol{\Pi}^*_0$ and $\boldsymbol{Q}^*_{t_0/r_0/v_0}$ were substituted for $-2\eta^*[\boldsymbol{\nabla}^*\boldsymbol{u}^*]^{(2)}$ and $-k^*_{t/r/v}T^*_{t/r/v}\boldsymbol{\nabla}^*(\ln T^*_{t/r/v})$. For the present study, we selected two criteria: one where $\hat{\Pi}_0$ and $\hat{Q}_{t_0}$ were taken as constants, and the other where $\hat{Q}_{t_0}$ and $\hat{Q}_{v_0}$ were taken as constants. This was done since the expressions (Eq. (50)) for $\hat{Q}_{t_0}$, $\hat{Q}_{r_0}$ and $\hat{Q}_{v_0}$ are mathematically similar.

A. Criteria 1: $\hat{\Pi}_0$ and $\hat{Q}_{t_0}$ are constant

The topological plots obtained for $\hat{\Pi}, \hat{Q}_t, \hat{Q}_r$ and $\hat{Q}_v$ for various values of $\hat{Q}_{t_0}$ and $\hat{\Pi}_0$ were found to be one among the plots shown in Fig. 1 and 2. The various cases of the constant values of $\hat{\Pi}_0$ and $\hat{Q}_{t_0}$ and their corresponding topologies have been tabulated in Table II and III.

Fig. 1 (a) shows the second-order vibrational heat flux $\hat{Q}_v$ as a function of first-order rotational and vibrational fluxes ($\hat{Q}_{r_0}$ and $\hat{Q}_{v_0}$) at $\hat{\Pi}_0 = 0, \hat{Q}_{t_0} = 0$. The vibrational heat flux surface exhibits a smooth, monotonic transition from negative to positive values. The fact that it isn't a flat 45-degree slope proves that the NCCR model does not treat vibrational heat flux as a simple linear function.

The most critical feature here is the saturation effect. While the NSF driving forces on the x and y axes span a massive range (± 20), the resulting NCCR flux is tightly constrained to roughly ± 3. The topology is not a flat plane (which would represent linear Newtonian/Fourier behavior) but a curved manifold, which is addressed as a "Nonlinear positive correlation". This demonstrates that as thermodynamic gradients become extreme, the resulting vibrational heat flux plateaus, naturally preventing the nonphysical singularities. The translational heat flux for any combination of first-order rotational and vibrational heat flux is zero if the first-order translational heat flux is assumed to be zero, as represented in Fig. 1 (b), even in the presence of high first-order shear stress ($\hat{\Pi}_0 = 20$). This illustrates a specific decoupling within the phase space.

The surface of $\hat{\Pi}$ at a positive first-order $\hat{Q}_{t_0}$ (=20) forms a downward-facing paraboloid referred to as a "Symmetric maxima" feature, as shown in Fig. 1 (c). The maximum value occurs at the origin. The dome in Fig. 1 (c) shows that as the gas gets further from equilibrium (moving toward the corners of the plots), the different transport mechanisms begin to interfere with one another. The perfect symmetry indicates that the coupling depends on the magnitudes of the NSF heat fluxes, not on their directions. Unlike $\hat{\Pi}$, the surface for $\hat{Q}_t$ flips for a negative $\hat{Q}_{t_0}$(=-20) as shown in 1 (d). The topology shows that increasing the magnitude of the rotational or vibrational heat fluxes increases the magnitude of the translational heat flux in this specific state.

The transition from planar to curved surfaces highlights a fundamental shift in the coupling of the fluxes. Figure 2 (e) and 2 (f) demonstrate that when the initial NSF parameter $\hat{\Pi}_0$ is non-zero and of high magnitude, the resulting NCCR fluxes exhibit a linear correlation. This indicates a regime where the transport phenomena are dominated by direct driving forces, leading to a predictable, first-order response. In contrast, when the parameter is minimized (as seen in Fig. 2 (g) and 2 (h) where $\hat{\Pi}_0 = 0$), the intrinsic nonlinearity of the NCCR model is revealed. The emergence

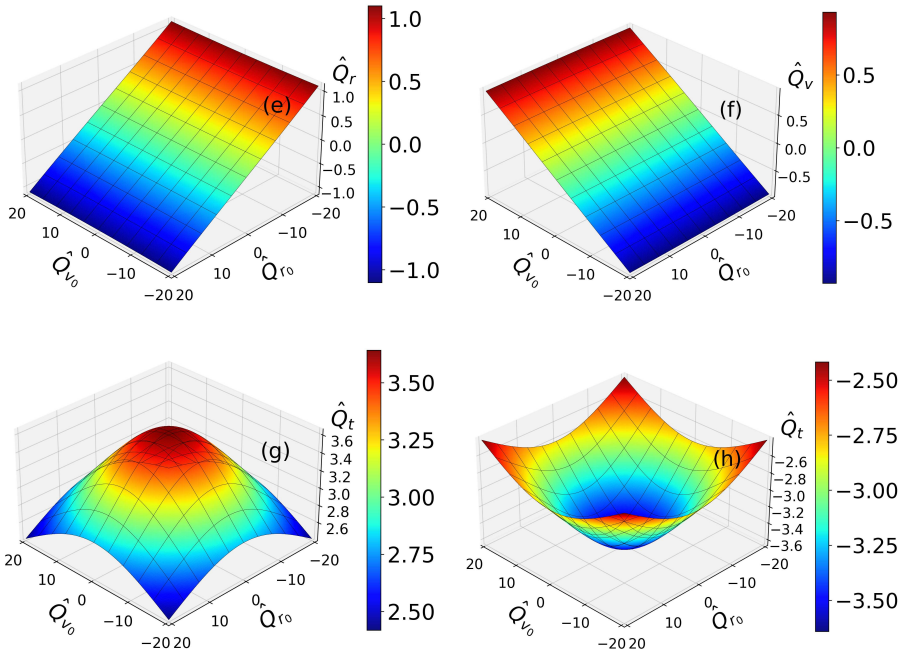

FIG. 2: Three-dimensional topologies of NCCR fluxes as a function of the constant values of NSF $\hat{\Pi}_0$ and NSF $\hat{Q}_{t_0}$, (e) Negative linear correlation ($\hat{\Pi}_0 = 20, \hat{Q}_{t_0} = 20$), (f) Positive linear correlation ($\hat{\Pi}_0 = -20, \hat{Q}_{t_0} = 0$), (g) Conical dome ($\hat{\Pi}_0 = 0, \hat{Q}_{t_0} = 20$), (h) Conical well ($\hat{\Pi}_0 = 0, \hat{Q}_{t_0} = -20$).

of the "Conical dome" and "Conical well" topologies suggests that at lower NSF base values, the interaction between the rotational ($\hat{Q}_{r_0}$) and vibrational ($\hat{Q}_{v_0}$) components becomes highly coupled, creating distinct extrema in the flux space. It is expected that the topological plots of $\hat{Q}_t$, $\hat{Q}_r$, and $\hat{Q}_v$ will be similar, as they are obtained using a similar set of equations. This is observed in the case of $\hat{Q}_r$ and $\hat{Q}_v$ for all values of $\hat{\Pi}_0$ and $\hat{Q}_{t_0}$ as tabulated in Table II and III. The apparent difference in the topologies of $\hat{Q}_t$ is due to the limitations of two-dimensional projections.

Figure 3 shows the three-dimensional plots for $\hat{\Pi}_0 = -20, 0$, and 20. The topological symmetry of $\hat{\Pi}$ with respect to all three heat fluxes is evident from Fig. 3(a) and 3(i) for $\hat{\Pi}_0 \neq 0$. A cross-section with respect to any of the axes provides a "Symmetric maxima" (Fig. 3(a)) or a "Symmetric minima" (Fig. 3(i)). For $\hat{\Pi}_0 = 0$, the $\hat{\Pi}$ is zero in the complete domain.

TABLE II: Topologies of $\hat{\Pi}$ and $\hat{Q}_t$ when $\hat{\Pi}_0, \hat{Q}_{t_0}$ are constants

$\hat{\Pi}_0 \rightarrow$ $\hat{Q}_{t_0} \downarrow$	-20	0	20
-20	$\hat{\Pi}$: Symmetric minima $\hat{Q}_t$: Symmetric minima	$\hat{\Pi}$: Zero value $\hat{Q}_t$: Conical well	$\hat{\Pi}$: Symmetric maxima $\hat{Q}_t$: Symmetric minima
0	$\hat{\Pi}$: Symmetric minima $\hat{Q}_t$: Zero value	$\hat{\Pi}$: Zero value $\hat{Q}_t$: Zero value	$\hat{\Pi}$: Symmetric maxima $\hat{Q}_t$: Zero value
20	$\hat{\Pi}$: Symmetric minima $\hat{Q}_t$: Symmetric maxima	$\hat{\Pi}$: Zero value $\hat{Q}_t$: Conical dome	$\hat{\Pi}$: Symmetric maxima $\hat{Q}_t$: Symmetric maxima

TABLE III: Topologies of $\hat{Q}_r$ and $\hat{Q}_v$ when $\hat{\Pi}_0, \hat{Q}_{t_0}$ are constants

$\hat{\Pi}_0 \rightarrow$ $\hat{Q}_{t_0} \downarrow$	-20	0	20
(-20 or 0 or 20)	Positive linear correlation	Nonlinear positive correlation	Negative linear correlation

The three-dimensional topologies allow us to visualize the variations of $\hat{Q}_{t_0}$. Its two-dimensional topologies are sections of the contour plots in Fig. 3(b), 3(f), and 3(j). The appearance of parallel planes in the contour plots of $\hat{Q}_t$ when $\hat{\Pi} \neq 0$ is due to the lower curvature values. The two-dimensional plots reveal this aspect as "Symmetric maxima/minima" topologies tabulated in Table II. The curvature gets magnified when $\hat{\Pi} = 0$ as shown in Fig. 3(f). The "Conical dome/well" topologies tabulated in Table II correspond to this observation. The similarity between the topologies of $\hat{Q}_r, \hat{Q}_v$, and $\hat{Q}_t$ is evident.

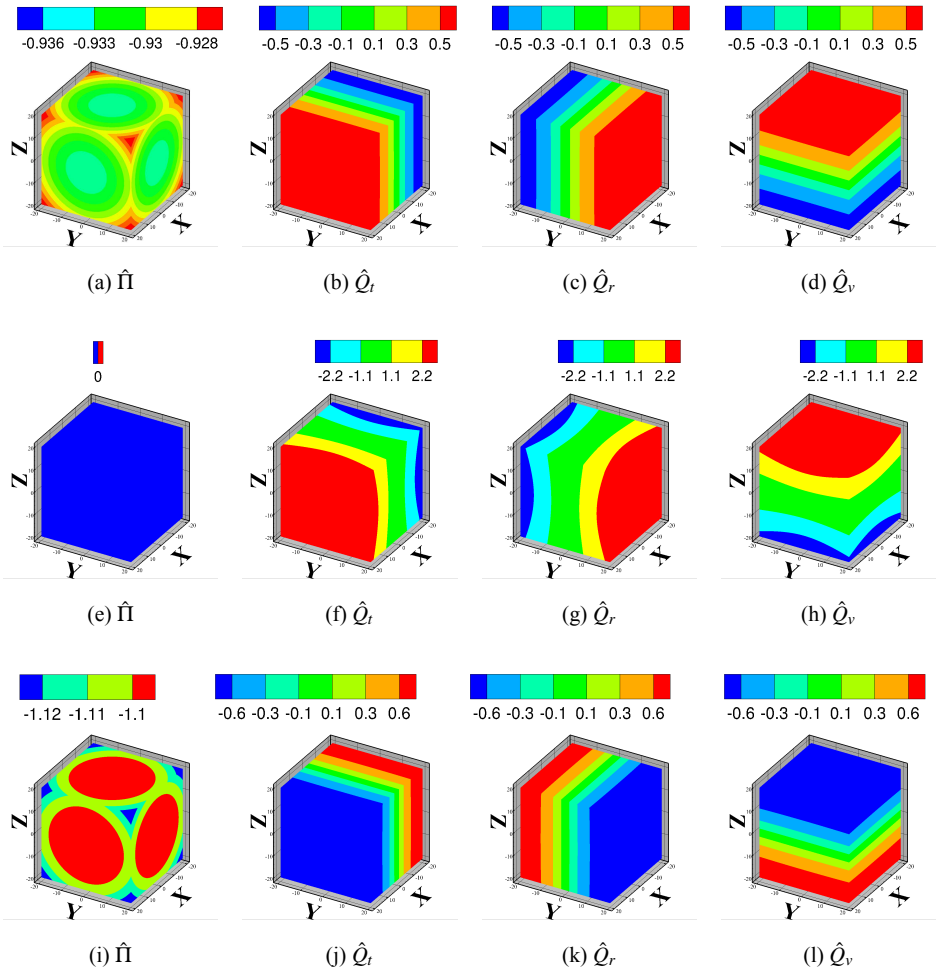

(a) $\hat{\Pi}$ (b) $\hat{Q}_t$ (c) $\hat{Q}_r$ (d) $\hat{Q}_v$

(e) $\hat{\Pi}$ (f) $\hat{Q}_t$ (g) $\hat{Q}_r$ (h) $\hat{Q}_v$

(i) $\hat{\Pi}$ (j) $\hat{Q}_t$ (k) $\hat{Q}_r$ (l) $\hat{Q}_v$

FIG. 3: Three-dimensional topologies of NCCR fluxes as a function of the constant values of NSF $\hat{\Pi}_0$ with $X = \hat{Q}_{t_0}$, $Y = \hat{Q}_{r_0}$, and $Z = \hat{Q}_{v_0}$ (Top row: $\hat{\Pi}_0 = -20$, Middle row: $\hat{\Pi}_0 = 0$, Last row: $\hat{\Pi}_0 = 20$)

TABLE IV: Topologies of $\hat{\Pi}$ and $\hat{Q}_r$ table when $\hat{Q}_{t_0}, \hat{Q}_{v_0}$ are constants

$\hat{Q}_{t_0} \downarrow$	$\hat{Q}_{v_0} \rightarrow -20$ or 0 or 20
-20 or 0 or 20	$\hat{\Pi}$: Nonlinear Slope, $\hat{Q}_r$: Twisted

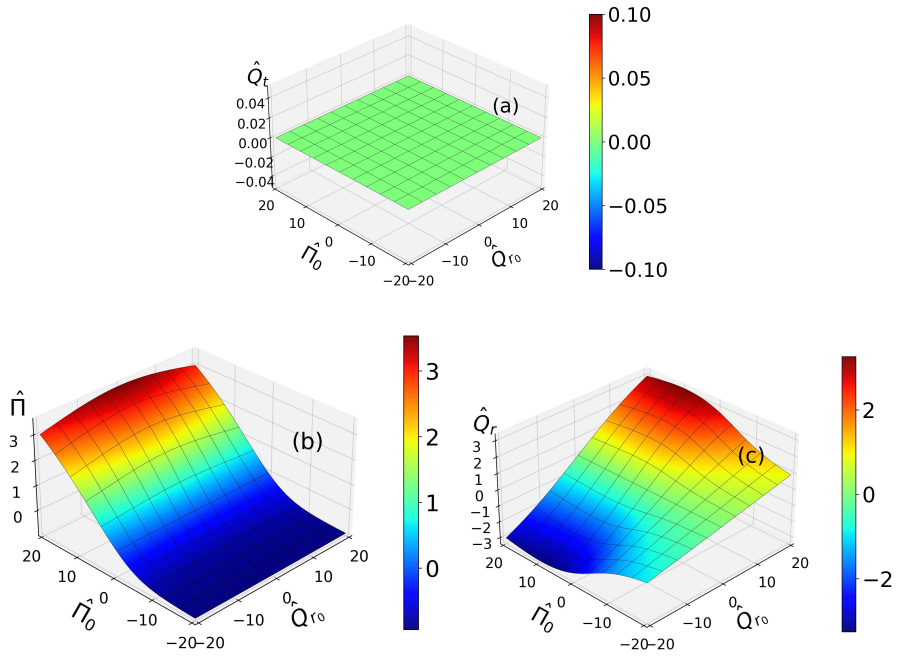

FIG. 4: Three-dimensional topologies of NCCR fluxes as a function of the constant values of NSF $\hat{Q}_{t_0}$ and NSF $\hat{Q}_{v_0}$, (a) Zero value ($\hat{Q}_{t_0} = 0, \hat{Q}_{v_0} = 20$), (b) Nonlinear slope ($\hat{Q}_{t_0} = 0, \hat{Q}_{v_0} = 20$), (c) Twisted ($\hat{Q}_{t_0} = 0, \hat{Q}_{v_0} = 20$)

B. Criteria 2: $\hat{Q}_{t_0}$ and $\hat{Q}_{v_0}$ are constant

The topological plots presented in Figs. 4 and 5 illustrate the nonlinear response of the NCCR fluxes $\hat{\Pi}, \hat{Q}_t, \hat{Q}_r$, and $\hat{Q}_v$ as functions of the corresponding NSF quantities. These plots are generated by varying $\hat{\Pi}_0, \hat{Q}_{t_0}, \hat{Q}_{r_0}$, and $\hat{Q}_{v_0}$, thereby mapping the NCCR response in a reduced parameter space. The different combinations of $\hat{Q}_{t_0}$ and $\hat{Q}_{v_0}$ produce a range of characteristic topologies, which are systematically categorized in Table IV and V. Physically, this representation highlights how the NCCR formulation transforms linear NSF inputs into nonlinear flux responses, thereby capturing deviations from local thermodynamic equilibrium in high-speed, rarefied flows.

Similar to the previous case, the two-dimensional topological plots obtained for $\hat{\Pi}, \hat{Q}_t, \hat{Q}_r$ and $\hat{Q}_v$ for various values of $\hat{Q}_{t_0}$ and $\hat{Q}_{v_0}$ were found to be one among the plots shown in Fig. 4 and 5.

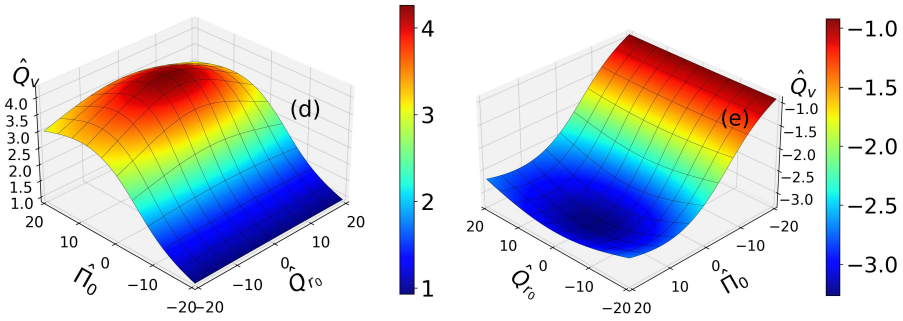

FIG. 5: Three-dimensional topologies of NCCR fluxes as a function of the constant values of NSF $\hat{Q}_{t_0}$ and NSF $\hat{Q}_{v_0}$, (d) Slope with dome ($\hat{Q}_{t_0} = 0, \hat{Q}_{v_0} = 20$), (e) Slope with well ($\hat{Q}_{t_0} = -20, \hat{Q}_{v_0} = -20$)

TABLE V: Topologies of $\hat{Q}_t, \hat{Q}_v$ when $\hat{Q}_{t_0}, \hat{Q}_{v_0}$ are constants

$\hat{Q}_{v_0} \rightarrow$ $\hat{Q}_{t_0} \downarrow$	-20	0	20
-20	$\hat{Q}_t$: Slope with well $\hat{Q}_v$: Slope with well	$\hat{Q}_t$: Slope with well $\hat{Q}_v$: Zero value	$\hat{Q}_t$: Slope with well $\hat{Q}_v$: Slope with dome
0	$\hat{Q}_t$: Zero value $\hat{Q}_v$: Slope with well	$\hat{Q}_t$: Zero value $\hat{Q}_v$: Zero value	$\hat{Q}_t$: Zero value $\hat{Q}_v$: Slope with dome
20	$\hat{Q}_t$: Slope with dome $\hat{Q}_v$: Slope with well	$\hat{Q}_t$: Slope with dome $\hat{Q}_v$: Zero value	$\hat{Q}_t$: Slope with dome $\hat{Q}_v$: Slope with dome

From Table IV, we observe that the topologies corresponding to $\hat{Q}_t$ exhibit distinct structural variations depending on the sign and magnitude of $\hat{Q}_{t_0}$. For $\hat{Q}_{t_0} = 0$, as shown in Fig. 4(a), the surface reduces to a flat plane at zero value, indicating that in the absence of a driving translational heat flux, the higher-order corrections vanish. When $\hat{Q}_{t_0}$ is negative, the topology develops a slope with a well-like structure. Conversely, for positive values of $\hat{Q}_{t_0}$, a dome-shaped topology

emerges. Physically, this suggests that the NCCR formulation can capture asymmetric transport behavior depending on the direction of the imposed gradient. A similar behavior is observed for the vibrational heat flux $\hat{Q}_v$, whose topology closely follows that of $\hat{Q}_t$, owing to the analogous mathematical structure of their governing equations.

In contrast, the topologies associated with $\hat{\Pi}$ and $\hat{Q}_r$, as shown in Fig. 4 (b) and Fig. 4 (c), display relatively weaker sensitivity to variations in $(\hat{Q}_{t_0}, \hat{Q}_{v_0})$. These surfaces are characterized by smoother slopes and mild twisting, indicating that the nonlinear corrections to these quantities are less influenced by the selected NSF heat-flux components. The $\hat{\Pi}$ surface signifies a saturation effect: at extreme values of the NSF flux, the NCCR response does not continue to grow but instead levels off. The "Twisted" topology in Fig. 4 (c) shows how the magnitude of the NCCR rotational heat flux enhances with the polarity of $\hat{\Pi}_0$. A saturation is observed as the magnitude of $\hat{Q}_{r_0}$ is increased or decreased. Figure 5 (d) and 5 (e) introduce a more complex interaction where the surfaces exhibit both a primary gradient (slope) and a localized curvature (dome or well). Along the $\hat{Q}_{r_0}$ axis, the surface forms a convex arch. This suggests that for any positive value of $\hat{\Pi}_0$, there is an optimal rotational heat flux that maximizes the vibrational response. A similar observation can be forwarded to the "Slope with well" topology in Fig. 5 (e).

The corresponding three-dimensional topologies for $\hat{Q}_{t_0} = -20, 0$, and 20 are given in Fig. 6 where $\hat{Q}_{v_0}$ is allowed to have continuous values and is not limited to $-20, 0$, and 20. The symmetry of $\hat{\Pi}$ with respect to $\hat{Q}_r$ and $\hat{Q}_v$ is evident from Fig. 6(a), 6(e), and 6(i) to be in the form of circular shaped contours at the centers. Similarly, the symmetry in $\hat{Q}_t$ with respect to $\hat{Q}_r$ and $\hat{Q}_v$ is evident in Fig. 6(b) and 6(j). In many of these volumes, we see nested ellipsoidal or spherical contours. This suggests that for a given $\hat{Q}_{t_0}$, there is an optimal point inside the $\hat{\Pi}_0$, $\hat{Q}_{r_0}$, and $\hat{Q}_{v_0}$ domain where the flux reaches an extrema. Further, the orthogonality of $\hat{Q}_r$ and $\hat{Q}_v$ is evident.

The topological characteristics observed in the NCCR fluxes have direct implications for predicting shock structures in non-equilibrium flows. In a shock layer, steep gradients in velocity, temperature, and internal energy modes lead to strong deviations from equilibrium, making linear constitutive relations inadequate. The observed asymmetry and anisotropy in the three-dimensional topologies indicate that fluxes respond differently depending on the direction and magnitude of the driving gradients. This behavior is critical to accurately capture shock profiles, where upstream and downstream conditions are inherently asymmetric. Most of the topological features observed in the current study are similar to those obtained with the two-temperature formulations. Topologies such as Nonlinear positive correlation, Twisted, Symmetric maxima, Slope with dome, and

Zero value are common in previous studies[53,56].

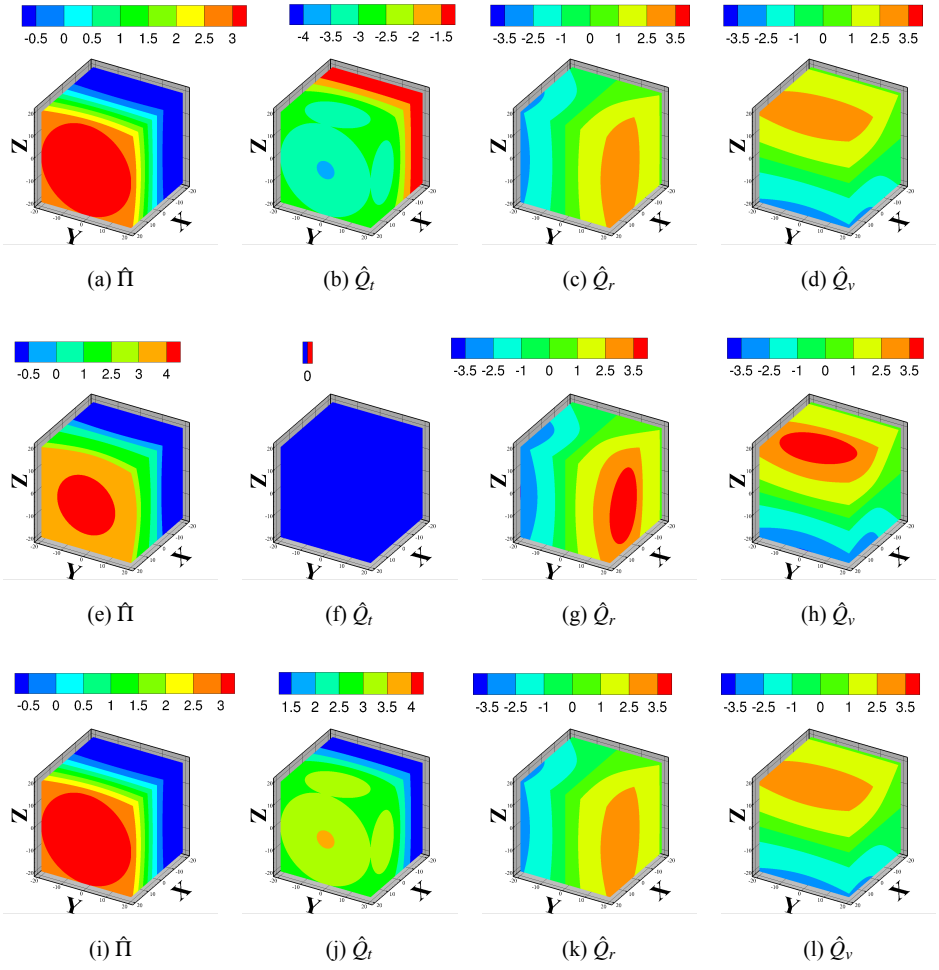

(a) $\hat{\Pi}$ (b) $\hat{Q}_t$ (c) $\hat{Q}_r$ (d) $\hat{Q}_v$

(e) $\hat{\Pi}$ (f) $\hat{Q}_t$ (g) $\hat{Q}_r$ (h) $\hat{Q}_v$

(i) $\hat{\Pi}$ (j) $\hat{Q}_t$ (k) $\hat{Q}_r$ (l) $\hat{Q}_v$

FIG. 6: Three-dimensional topologies of NCCR fluxes as a function of the constant values of NSF $\hat{Q}_{t_0}$ with $X = \hat{\Pi}_0$, $Y = \hat{Q}_{r_0}$, and $Z = \hat{Q}_{v_0}$ (Top row: $\hat{Q}_{t_0} = -20$, Middle row: $\hat{Q}_{t_0} = 0$, Last row: $\hat{Q}_{t_0} = 20$)

IV. RESULTS AND DISCUSSION

Shock structure analysis is often utilized to study non-equilibrium phenomena in gases. The infinitely long one-dimensional domain used for shock-structure simulation has no physical boundaries, thereby simplifying the analysis. The degree of non-equilibrium can easily be controlled by varying the upstream Mach number. A shock front typically divides the flow field into the upstream and the downstream regions. The properties in these two regions are connected through Rankine-Hugoniot (RH) relations[74].

The gas in the far upstream and downstream regions is usually assumed to be in thermal equilibrium. The majority of the non-equilibrium relaxation phenomena are observed in a narrow region of the shock structure, which spans over a length of the order of a few mean free paths. While this may be true for translational and rotational energies, it does not apply to vibrational energy because the translational-vibrational relaxation process is slower. Vibrational relaxation requires more collisions to reach equilibrium. Its relaxation zone can extend far behind the shock front.

Several studies[34] have shown that the relaxation of various internal modes follows the following order: translational, rotational, and then vibrational. However, for most applications, rotational relaxation is comparable to translational relaxation. It is usually considered to be in equilibrium with it, and a common temperature is assigned for the combined energy distribution. The two-temperature model of Park[30] is based on such an assumption. However, there have been cases[40] where the difference between the rotational and the translational modes is substantial. The assumption of a common trans-rotational temperature in such cases is not an accurate model.

$$\frac{T_1}{T_2} = \left[\frac{7}{2} + \frac{\gamma_2 M_2^2}{2} + \frac{(\theta_v/T_2)}{\{\exp(\theta_v/T_2)-1\}}\right] \Bigg/ \left[\frac{7}{2} + \frac{\gamma_1 M_1^2}{2}\right] \tag{52}$$

$$\gamma_2 = \left[\frac{7}{2} + \left\{\frac{(\theta_v/2T_2)}{\sinh(\theta_v/2T_2)}\right\}^2\right] \Bigg/ \left[\frac{5}{2} + \left\{\frac{(\theta_v/2T_2)}{\sinh(\theta_v/2T_2)}\right\}^2\right] \tag{53}$$

$$\frac{M_2}{M_1} = \frac{(1+\gamma_2 M_2^2)}{(1+\gamma_1 M_1^2)}\sqrt{\frac{\gamma_1 T_2}{\gamma_2 T_1}} \tag{54}$$

The current study employed the standard temperature and pressure values $(273.15\,\mathrm{K}, 101325\,\mathrm{Pa})$, as the upstream state (subscript '1'). At such low temperatures, the higher vibrational states are not populated. However, the downstream temperatures are high enough (at Mach 10 and 15) for vibrational excitation. Since the heat capacity of the gas does not remain constant in the shock region

due to the involvement of the vibrational mode, the generalized Rankine-Hugoniot conditions[53] (Eq. (IV)) were used to calculate the downstream parameters (subscript '2').

Equations. (25)-(27) require C_p values for various degrees of freedom. They were evaluated using the following relations[75,76]:

$$\begin{aligned} C_{p(t)} &= C_{v(t)} + R = R\left(\frac{3}{2}+1\right), \\ C_{p(r)} &= C_{v(r)} = R, \qquad C_{p(v)} = C_{v(v)} = R\left\{\frac{\theta_v/(2T)}{\sinh(\theta_v/(2T))}\right\}^2. \end{aligned} \tag{55}$$

The thermal conductivities (k_t, k_r, k_v) were calculated using the definition of the Prandtl number $(Pr = \eta C_p/k)$, which was assumed to be equal for each of the energy modes. The inverse power law collision model was used to model intermolecular collisions. This assumption led to the following relation between the coefficient of viscosity and the temperature:

$$\eta = \eta_{ref}\left(\frac{T_{ref}}{T}\right)^s \quad \begin{cases} s = 0.5, \text{ Hard sphere model} \\ s = 0.75, \text{ Power Law model} \\ s = 1.0, \text{ Maxwell's model} \end{cases} \tag{56}$$

where η_{ref} is the reference value of the viscosity at some reference temperature T_{ref}. The exponent s could be varied to modify the degree of squishiness of the intermolecular interaction.

The equations were discretized and solved numerically on a computational domain consisting of a grid of 1,500 cells. A domain length of 150 times the mean free path (λ_1) was used for most of the study. The convective terms were solved using the finite volume scheme of the Liou and Steffen[77] Riemann solver. The flux terms were discretized using the central difference scheme. An explicit Euler scheme was used for time stepping till the steady state was reached. The NCCR equations require a solution to a nonlinear equation, which was solved for the present study using the Newton-Raphson method. The simulation using the NCCR incurs a higher computational cost compared to the NSF formulation. However, the time and computational resources required for NCCR were still much lower than those for DSMC simulations.

It should be noted that the present three-temperature NCCR formulation is developed upon the foundation of our previously established NCCR framework[68,53], whose predictive capability for shock-wave structures has been validated against available experimental measurements[78]. While such experimental data provide confidence in the underlying hydrodynamic formulation,

direct measurements of translational, rotational, and vibrational temperatures in rarefied hypersonic shock waves remain extremely limited owing to the challenges associated with obtaining spatially and temporally resolved diagnostics in strongly nonequilibrium flow environments[79]. Consequently, Direct Simulation Monte Carlo (DSMC) results, which have been extensively validated against experimental data for rarefied gas flows[80], are employed in the present work as a high-fidelity benchmark for assessing the multi-temperature predictions of the proposed model.

A. Comparison with DSMC results

The results are presented at different Mach numbers in normalized coordinates. Data normalization was performed to enable better comparison of various profiles of a particular property at different Mach numbers. Normalization was performed using the upstream and downstream values. The study employed nitrogen as the working gas, which was assumed to follow the power-law model for interaction ($s = 0.75$), with relaxation parameters set to those of nitrogen gas. The properties of nitrogen gas used in the study are tabulated in Table VI.

TABLE VI: N_2 gas properties

$T'\,(K)$	Z_r^∞	$\theta_v\,(K)$	$\theta_r\,(K)$	$T_{ref}\,(K)$	$\eta_{ref}\,(Ns/m^2)$	Pr	$R\,(J/kgK)$
80	15.7	3390	2.9	273.15	1.66×10^{-5}	0.72	296.72

Two sets of DSMC simulations[81] were performed to obtain data related to two-temperature (Mach 15) and three-temperature formulations (Mach 10 and 15). The collisions were modeled using Maxwell's model (MW) for the two-temperature case[53] and the variable hard sphere (VHS) for the three-temperature case. The inelastic rotational and vibrational energy exchanges were treated using the Larsen–Borgnakke (LB) model with constant rotational and vibrational relaxation parameters, which were $Z_r = 1, Z_v = 50$ for the MW model and $Z_r = 5, Z_v = 50$ for the VHS model. The model parameters were specified as $\omega = 0.75$ (VHS) and $\omega = 1.0$ (MW) for $T_{ref} =$ 273 K, and $d_{ref} = 4.74$Å. The initial conditions on both the upstream and downstream sides of the shock tube were identical to those employed in the CFD simulations. The DSMC time step was selected as a fraction of the mean collision time evaluated from the upstream-side conditions, and the cell size was taken to be 0.4λ. To minimize the random-walk effect, which can lead to

artificial broadening of the shock structure, a very large number of representative particles was used, corresponding to approximately 3×10^6 particles per cell in the driver section. Although this substantially increased the computational expense, it ensured that the computed shock structure remained free from distortions associated with artificial stabilization techniques. The upstream and downstream properties used in the simulations are tabulated in Table VII.

TABLE VII: Upstream parameters at Mach 10 and 15

Mach	T_1 (K)	T_2 (K)	p_1 (Pa)	p_2 (Pa)	ρ_1 (kg m^{-3})	ρ_2 (kg m^{-3})
10.0	273.15	4706.90	101325.0	12266826.81	1.25	8.78
15.0	273.15	9958.21	101325.0	27771212.87	1.25	9.39

It is important to note that Srivastava *et al.*[56] compared their simulation results with the MD results of Valentini *et al.*[63] for Mach numbers 7 and 12.7. The upstream temperatures considered in the MD simulation were 28.3 K and 9.0 K, respectively. Since the vibrational mode only becomes prominent at high temperatures, the MD simulation results reported in Valentini *et al.*[63] cannot be used for comparison with the present work. Further, the comparison in Srivastava *et al.* with the DSMC results of Yuan *et al.*[82] at Mach 5 and 10 was limited to the translational and rotational degrees of freedom. Since the present study incorporates the vibrational temperature in addition to the translational and rotational temperatures, it was more appropriate to compare it with DSMC results available for the three temperatures at Mach numbers 10 and 15.

Figure 7(a) compares the density plots obtained using the 2T, 3T NCCR, and DSMC simulations at Mach 15 for the Maxwell model[53]. The profiles obtained with 2T and 3T formulations are close to the DSMC simulation results, with the 3T formulation being more accurate in the upstream region. Figure 7(b) shows the translational temperature profile for the 3T and DSMC formulations and the trans-rotational temperature for the 2T formulation. The 3T model appears to predict a slightly higher peak temperature than the 2T model, which aligns more closely with the DSMC peak height, even though the spatial location is slightly shifted.

Figure 8 (a) compares the rotational temperature obtained using the 3T formulation and the trans-rotational temperature obtained using the 2T formulation with the rotational temperature of DSMC simulations at Mach 15 for the Maxwell model[53]. The peak rotational temperature is well

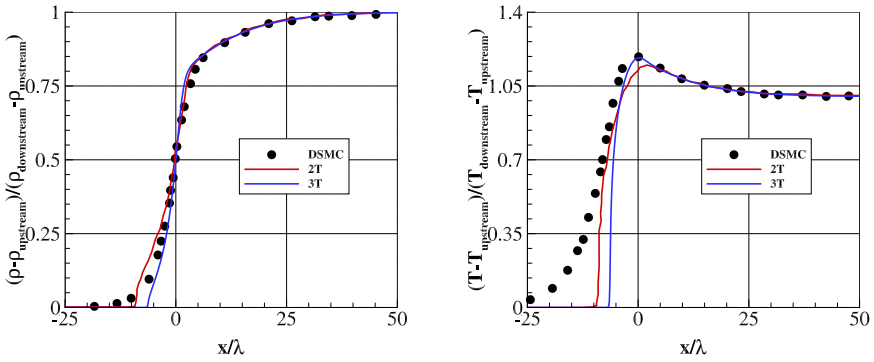

(a) (b)

FIG. 7: Comparison of (a) density and (b) translational temperature profiles predicted by DSMC, 2T and 3T NCCR formulations for Mach number $M = 15$ $(s = 1)$.

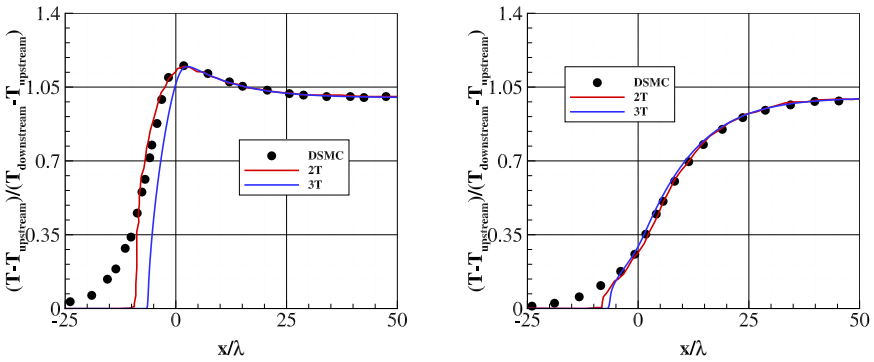

(a) (b)

FIG. 8: Comparison of (a) rotational and (b) vibrational temperature profiles predicted by DSMC, 2T and 3T NCCR formulations for Mach number $M = 15$ $(s = 1)$.

captured by the 2T and 3T formulations. The trans-rotational temperature profile from the 2T formulation is closer to the DSMC rotational temperature plot as compared to the rotational temperature plot of the 3T formulation. However, it lies between the DSMC translational and rotational

temperature profiles, which are close to each other because the rotational collision number ($Z_r = 1$) is small. For a substantial value of Z_r, the trans-rotational temperature profile will deviate significantly from translational and rotational temperatures. Further, the greater discrepancy between the DSMC simulations and the continuum results near the upstream region is expected, as DSMC simulations are equivalent to solving the infinite set of moment equations. In contrast, the continuum approach in the present case is limited to a finite set of moment equations with second-order accuracy. Figure 8 (b) compares the vibrational temperature profile obtained using the three formulations. The 3T vibrational temperature profile is closer to that of the 2T formulation and to the DSMC simulation profile for a considerable region.

Figure 9 compares the three-temperature profiles calculated using the NCCR, NSF, and the DSMC formulations for Mach 10. The NCCR formulation provides a better match to the DSMC results than the NSF profiles do. Similarly, the temperature profiles for Mach 15 are shown in Fig. 10. The NCCR formulation provides improved predictions of rotational and vibrational temperatures near the upstream region. The translational temperature profile bulges in the middle to match the DSMC profile at both Mach numbers.

The temperature profiles in Fig. 9 and 10 were obtained using a constant value of collision numbers for both the rotational ($Z_r^{DSMC} = 5$) and vibrational ($Z_v^{DSMC} = 50$) modes in DSMC simulations. The relationship between Z values for the continuum and particle approaches is given using the following formula.

$$Z_{v/r}^{DSMC} = \frac{\zeta_t}{\zeta_t + \zeta_{v/r}} Z_{v/r}^{CONT} \quad \text{where} \quad \zeta_i = \frac{2E_i(T_i)}{RT_i} \tag{57}$$

where ζ_i is the degree of freedom of i^{th} mode. The relaxation times were calculated using Eq. (6) and the source terms were modeled using the Landau-Teller formula (Eq. (8)), with no energy exchange between the rotational and vibrational modes. The upstream conditions used for the simulation are listed in Table VII, and the properties of nitrogen gas are listed in Table VI.

A multi-temperature approach allows the comparison of temperature peaks for translational and rotational modes. Since the energy content of rotational and vibrational modes is higher for NCCR near the upstream region, the peak translational temperature is lower as compared to the peak translational temperature predicted by the NSF formulation. The DSMC simulation, however, predicts a higher peak for the translational temperature for both Mach numbers. The CPU time required for NCCR simulations was $\sim$ 2.5 hours (2.59 hrs for Mach 10 and 2.52 hrs for Mach 15) and for NSF simulations was $\sim$ 1.60 hours (1.62 hrs for Mach 10 and 1.59 hrs for Mach 15).

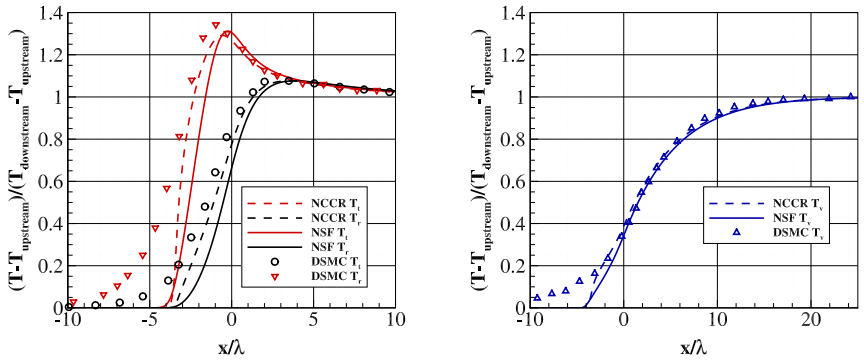

FIG. 9: Comparison of temperature profiles predicted by DSMC, NSF, and NCCR for Mach number $M = 10$ for power law molecules ($s = 0.75$).

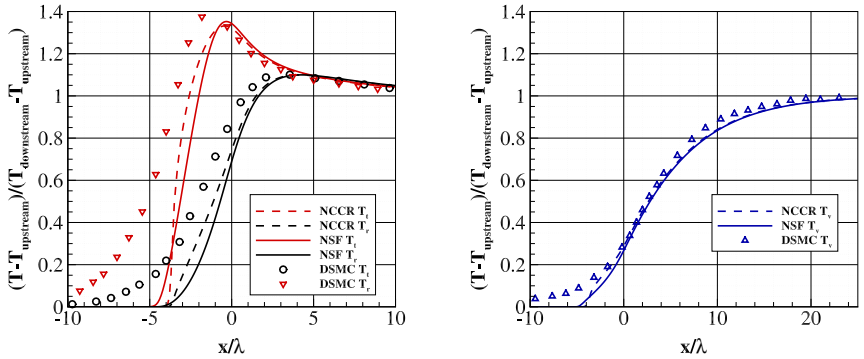

FIG. 10: Comparison of temperature profiles predicted by DSMC, NSF, and NCCR for Mach number $M = 15$ for power law molecules ($s = 0.75$).

The DSMC simulation took ~ 312.88 hours for Mach 10 and ~ 372.02 hours for Mach 15. The simulations were performed on an Intel(R) Xeon(R) Silver 4214 CPU @ 2.20 GHz.

The plots shown in Fig. 11 were calculated using the NSF and NCCR solutions and represent projections of the shock structure phase space onto the hyperspaces discussed in the previous section. The non-dimensional non-conserved moments, Π', Q'_t, Q'_r, and Q'_v, are defined using the

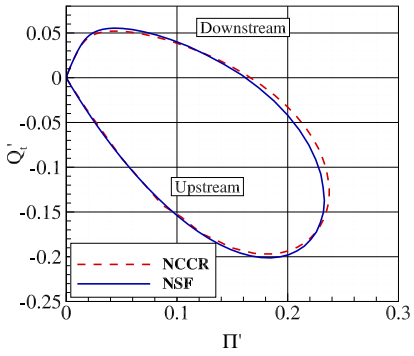

(a) Π' vs Q'_t

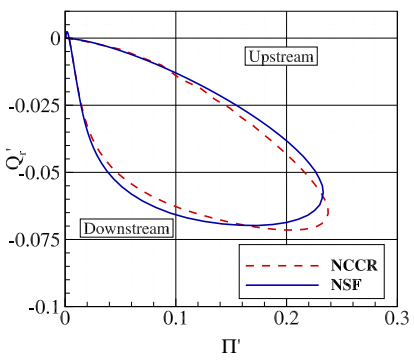

(b) Π' vs Q'_r

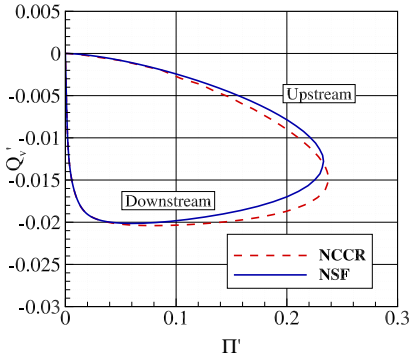

(c) Π' vs Q'_v

FIG. 11: The plots of Π' vs Q'_t for NSF and NCCR at Mach 15 (Power law model $(s = 0.75)$)

following formula:

$$\Pi' = \frac{\Pi}{\rho_1 U_1^2 + P_1}, \quad Q'_{t/r/v} = \frac{Q_{t/r/v}}{U_1\left(\frac{1}{2}\rho_1 U_1^2 + P_1 \frac{\gamma_1}{(\gamma_1 - 1)}\right)} \tag{58}$$

It can be inferred from Fig. 11 that the variation in Q'_t, Q'_r and Q'_v with respect to Π' has different relations at different points in the shock structure. Additionally, the peak translational and rotational temperatures exceed the downstream equilibrium temperature. This leads to the curves spanning both the negative and positive quadrants of the heat fluxes. The positive regions in Figs.

12(b) and 12(c) also reflect the same phenomena in translational and rotational temperatures. Since the translational-vibrational relaxation is much slower, the vibrational temperature never exceeds the downstream temperature, which can also be observed from the Q'_v with respect to the Π' line plot. It is noteworthy that the difference in non-conserved moments across the shock structure, as obtained from the NSF and NCCR, is prominently captured in these phase space diagrams. This is in contrast to the shock structure profiles shown in Fig. 9, where the relaxation dominates over viscous effects. Figs. 11 and 12 show that the peak heat flux calculated using NCCR is lower than that from NSF, and the opposite is true for the rotational and the vibrational heat fluxes, as well as the viscous stress.

These simulations employed constant values for the rotational and vibrational collision numbers. It was assumed that the number of collisions required for rotational and vibrational equilibration with the translational mode of energy is constant. In practice, the relaxation is strongly temperature-dependent. Moreover, the exchange of energy between the rotational and vibrational modes has been observed at higher temperatures, which should be accounted for. Both of these phenomena are discussed in the following subsections.

B. Effect of Temperature-dependent Relaxation models

Figure 13 (a) shows the effect of rotational relaxation time on the temperature profiles, predicted using Parker's and Park's approaches, for a constant value of vibrational collision number ($Z_v = 50$). Since the relaxation models are a function of the translational temperature, it is important to observe the change in $p\tau_r$ values with respect to the translational temperature as shown in Fig. 13 (b). Around a temperature value of 1200 K, the $p\tau_r$ predicted using Park's formulation exceeds that of Parker's formulation. Since, for the present case at Mach 15, the temperature change ranges from 273.15 K to 9958.21 K as given in Table VII, the majority of the flow region is above the value of 1200 K and hence the rotational relaxation is slower for Park's model compared to that of the Parker's models as seen in Fig. 13. This slower relaxation of the rotational mode increases the maximum translational temperature and widens the shock region. The vibrational relaxation is not much affected since a constant value of Z_v was taken, and no exchange of energy is allowed between the rotational and the vibrational mode.

Next, the effect of temperature-dependent vibrational relaxation time was employed for the previous case using the Millikan-White formulation with Park's correction (Eq. (10)). Fig. 14

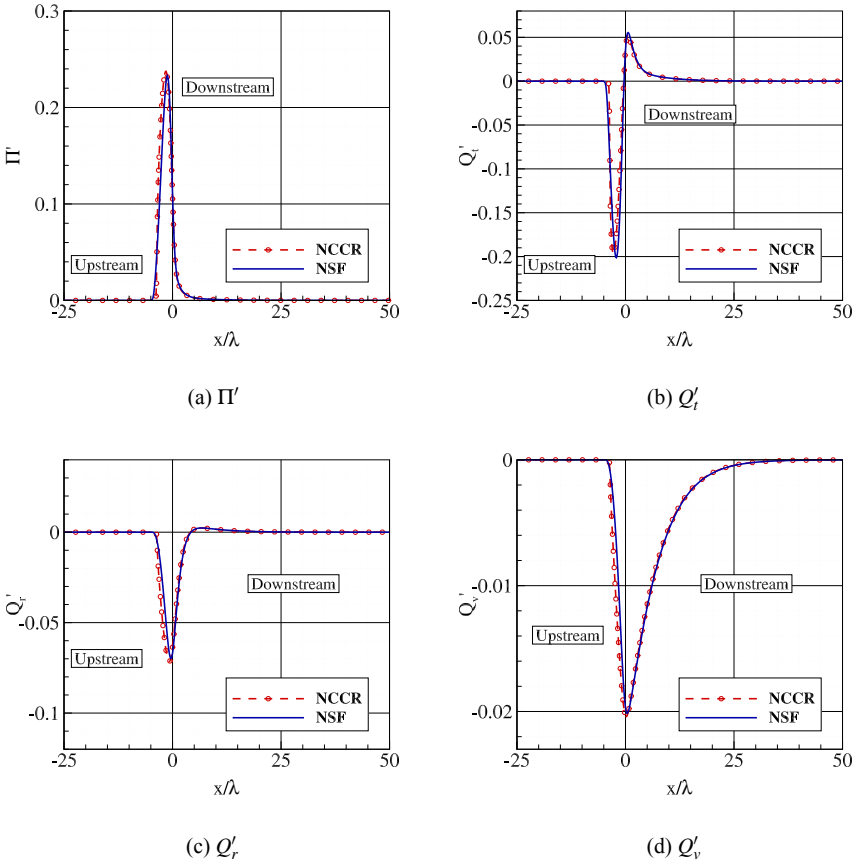

(a) Π' (b) Q_t'

(c) Q_r' (d) Q_v'

FIG. 12: Comparison of non-dimensionalized viscous stress and heat flux profiles predicted by NSF and NCCR for Mach number 15 (Power law model $(s = 0.75)$)

(a) shows the temperature profile obtained for the Mach 15 shock structure using temperature-dependent rotational and vibrational relaxation models. The exchange of energy between the rotational and vibrational modes is still absent. Figure 14 (b) shows the variation in vibrational relaxation time, which decreases with an increase in temperature. On comparing this with Fig. 13 (b), it is expected that the rotational relaxation time will exceed the vibrational relaxation time at some value of translational temperature. In the Park's model, this happens at a translational temperature of $\sim$ 13000 K, whereas it occurs at a still higher temperature in Parker's model. Since the

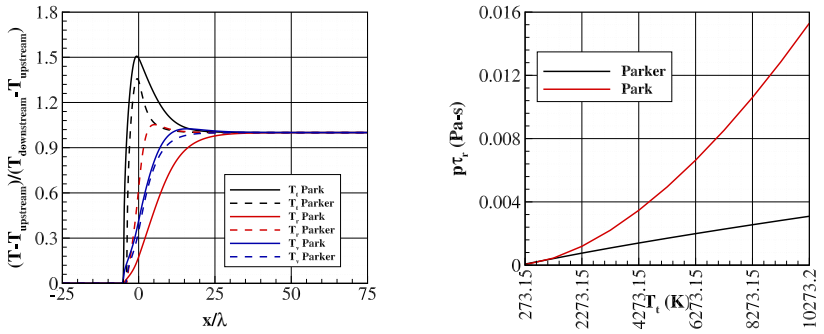

(a) (b)

FIG. 13: Comparison of (a) temperature profiles obtained using the Parker and Park approaches for NCCR formulation at Mach 15 for power law ($s = 0.75$) molecules, and (b) the variation of $p\tau_r$ for Parker and Park formulations.

crossover temperature exceeds the range encountered in the present case, the vibrational relaxation time remains greater than the rotational relaxation time throughout the shock region.

A comparison between the temperature profiles predicted using Parker's model, as shown in Fig. 13 and 14, reveals no significant change in the translational and rotational temperatures. In contrast, the vibrational temperature is broader in the present case. This is consistent with the current model, which predicts a larger vibrational relaxation time. A similar observation can be made for the Park's model, where the vibrational temperature profile broadens.

C. Energy exchange between rotational and vibrational modes

Figure 15 shows a comparison of the temperature profiles for the Mach 15 shock structure for power law gas ($s = 0.75$) using NCCR for cases where the energy exchanges between the rotational and vibrational modes were allowed and for those when these were not allowed. The relaxation models employed for both cases were Park's formula for the rotational relaxation time and the Millikan-White formula with Park's correction for the vibrational relaxation time. Significant deviations were observed in the vibrational relaxation profiles, whereas the rotational temperature relaxation profiles did not change appreciably. Moreover, the peak translational temperature was

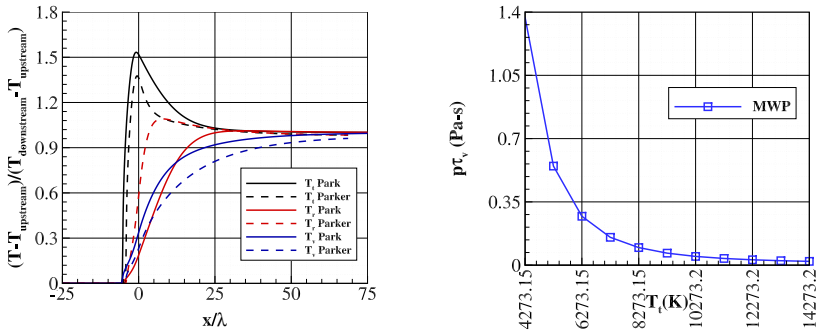

(a) (b)

FIG. 14: Comparison of (a) temperature profiles obtained using the Parker and Park approaches for NCCR formulation at Mach 15 for power law $(s = 0.75)$ molecules and (b) the variation of $p\tau_v$ for MWP relaxation model.

also the same for both cases.

Allowing energy exchange between rotational and vibrational modes offers an additional way for energy to flow between modes, in addition to the exchange with the translational mode. Fig. 15 shows the slow energy exchange between the vibrational and translational modes when energy exchange is allowed. A smaller deviation can also be observed in the rotational profiles for the two cases, indicating energy transfer from the rotational to the vibrational mode.

V. CONCLUSION

A new set of second-order constitutive relations based on a three-temperature framework is proposed as an extension of the Nonlinear Coupled Constitutive Relations (NCCR) to investigate non-equilibrium phenomena in shock structures at high Mach numbers. This formulation enables a more realistic representation of energy redistribution among internal degrees of freedom. The energy associated with each mode plays a crucial role in governing dependent phenomena such as dissociation, which is strongly influenced by the vibrational temperature. Furthermore, studies on shock standoff distance have shown that the common assumption of rotational–translational equilibrium can introduce significant inaccuracies when predicting flow properties under strongly

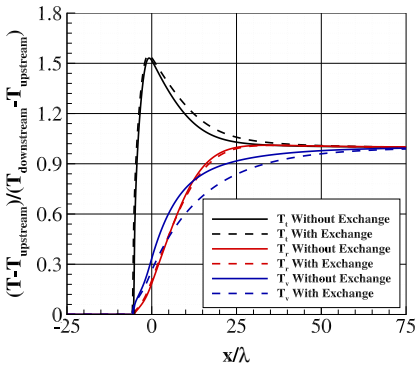

FIG. 15: Temperature profile comparison when energy exchange between rotational and vibrational modes was allowed and when it was restricted.

non-equilibrium conditions.

The two-temperature model offers a simplified description when internal energy modes can be grouped into two categories. Typically, translational modes are assumed to equilibrate rapidly, while the remaining modes evolve over longer timescales. In conventional approaches, rotational modes are often grouped with translational modes, whereas vibrational modes are associated with chemical reactions and dissociation processes. However, in rarefied environments, even rotational modes may exhibit delayed equilibration, necessitating multi-temperature formulations to improve accuracy.

An important advantage of the three-temperature model is its ability to resolve the energy content of each degree of freedom independently. This distinction is particularly important in applications where physical processes are sensitive to the excitation of specific modes. Notably, rotational and translational modes may attain different peak values, highlighting the limitations of equilibrium assumptions and reinforcing the need for multi-temperature modeling.

The present study compared predictions from the NCCR framework with Direct Simulation Monte Carlo (DSMC) results for the three-temperature model. While the overall trends were comparable to those of two-temperature formulations, the three-temperature approach demonstrated superior ability to accurately capture peak temperatures, which are often inadequately represented in simpler models. To ensure realistic modeling of the energy exchange and relaxation processes,

established formulations were employed, including the Parker and Park models for rotational relaxation and the Millikan–White model with Park's high-temperature correction for vibrational relaxation. In addition, a focused analysis was conducted to assess the impact of rotational–vibrational coupling by comparing results with and without such interactions.

Topological plots were used to investigate the nonlinear characteristics of the proposed model and to enable comparison with the Navier–Stokes–Fourier (NSF) formulation. The analysis was carried out in a five-dimensional parameter space, with lower-dimensional representations obtained by fixing selected variables. These visualizations provide insight into the influence of higher-order effects introduced by the NCCR framework and demonstrate its effectiveness in capturing strongly non-equilibrium behavior. Overall, the topological analysis underscores the inherently nonlinear nature of the NCCR formulation.

Despite its advantages, the three-temperature model remains an approximation. It is based on quasi-equilibrium assumptions within each energy mode and relies heavily on empirical relaxation models. Consequently, its accuracy may be limited in highly rarefied flows, high-temperature regimes involving dissociation and ionization, and situations where detailed state-to-state energy transitions are significant.

The present study can be extended in several directions to enhance physical realism. At elevated temperatures, increased vibrational excitation promotes dissociation, making its inclusion a natural progression. Additionally, ionization and chemical reactions may occur simultaneously, leading to strongly coupled multi-physics interactions. As temperature increases, rotational relaxation rates tend to decrease, while vibrational relaxation rates tend to increase, potentially leading to resonance-like energy exchange between modes. Accurate representation of such coupling requires more advanced relaxation models. Furthermore, the precise determination of relaxation times remains an open research challenge, as it directly influences temperature evolution and energy redistribution among modes. Incorporating more reliable relaxation formulations can therefore significantly improve the predictive capability of non-equilibrium flow models.

ACKNOWLEDGEMENTS

R.S.M. was supported by the National Research Foundation of Korea (NRF) Grant funded by the Ministry of Science and ICT (No. RS-2024-00397400) and the Korea AeroSpace Administration (No. RS-2022-NR067079, Future Space Education Center), South Korea.

AUTHOR DECLARATIONS

Conflict of Interest

The authors have no conflicts to disclose.

DATA AVAILABILITY

The data that support the findings of this study are available from the corresponding author upon request.

REFERENCES

[1]M. E. Holloway, K. M. Hanquist, and I. D. Boyd, "Assessment of thermochemistry modeling for hypersonic flow over a double cone," Journal of Thermophysics and Heat Transfer **34**, 538–547 (2020), https://doi.org/10.2514/1.T5792.

[2]M. Yu, Z. Qiu, B. Zhong, and Y. Takahashi, "Numerical simulation of thermochemical non-equilibrium flow-field characteristics around a hypersonic atmospheric reentry vehicle," Physics of Fluids **34**, 126103 (2022), https://doi.org/10.1063/5.0131460.

[3]T. Morimoto and K. Kinefuchi, "Effect of the vehicle nose radius on radio wave–plasma interference in hypersonic flight," Physics of Plasmas **32**, 063901 (2025), https://doi.org/10.1063/5.0242370.

[4]V. O. Knudsen, "The absorption of sound in gases," The Journal of the Acoustical Society of America **3**, 199–204 (1935), https://doi.org/10.1121/1.1915738.

[5]G. G. Stokes, "On the theories of the internal friction of fluids in motion, and of the equilibrium and motion of elastic solids," Transactions of the Cambridge Philosophical Society **8**, 287–305 (1845), https://doi.org/10.1017/CBO9780511702242.005.

[6]G. W. Pierce, "Piezoelectric crystal oscillators applied to the precision measurement of the velocity of sound in air and CO_2 at high frequencies," in *Proceedings of the American Academy of Arts and Sciences*, Vol. 60 (JSTOR, 1925) pp. 271–302, https://doi.org/10.2307/25130055.

[7]K. F. Herzfeld and F. O. Rice, "Dispersion and absorption of high frequency sound waves," Physical Review **31**, 691–695 (1928), https://doi.org/10.1103/PhysRev.31.691.

[8]H. O. Kneser, "The interpretation of the anomalous sound-absorption in air and oxygen in terms of molecular collisions," The Journal of the Acoustical Society of America **5**, 122–126 (1933), https://doi.org/10.1121/1.1915639.

[9]"On the theory of sound dispersion," in *Collected Papers of L.D. Landau*, edited by D. T. Haar (Pergamon, 1965) pp. 147–153, https://doi.org/10.1016/B978-0-08-010586-4.50027-4.

[10]H. A. Bethe and E. Teller, "Deviations from thermal equilibrium in shock waves," Tech. Rep. (Ballistics Research Laboratory, MD, NP-4898; BRL-X-117, 1953) https://www.osti.gov/servlets/purl/4420349.

[11]R. N. Schwartz, Z. I. Slawsky, and K. F. Herzfeld, "Calculation of vibrational relaxation times in gases," The Journal of Chemical Physics **20**, 1591–1599 (1952), https://doi.org/10.1063/1.1700221.

[12]R. J. Rubin and K. E. Shuler, "Relaxation of vibrational nonequilibrium distributions. I. Collisional relaxation of a system of harmonic oscillators," The Journal of Chemical Physics **25**, 59–67 (1956), https://doi.org/10.1063/1.1742849.

[13]R. J. Rubin and K. E. Shuler, "Relaxation of vibrational nonequilibrium distributions. II. The effect of the collisional transition probabilities on the relaxation behavior," The Journal of Chemical Physics **25**, 68–74 (1956), https://doi.org/10.1063/1.1742850.

[14]V. Blackman, "Vibrational relaxation in oxygen and nitrogen," Journal of Fluid Mechanics **1**, 61–85 (1956), https://doi.org/10.1017/S0022112056000056.

[15]D. Sette, A. Busala, and J. Hubbard, "Energy transfer by collisions in vapors of chlorinated methanes," The Journal of Chemical Physics **23**, 787–793 (1955), https://doi.org/10.1063/1.1742123.

[16]Y. Miyahara and E. G. Richardson, "Ultrasonic relaxation in freon vapors," The Journal of the Acoustical Society of America **28**, 1016–1019 (1956), https://doi.org/10.1121/1.1908541.

[17]P. D. Edmonds and J. Lamb, "Vibrational relaxation times of a number of polyatomic gases derived from measurements of acoustic absorption," in *Proceedings of the Physical Society*, Vol. 72 (IOP Publishing, 1958) pp. 940–948, https://doi.org/10.1088/0370-1328/72/6/302.

[18]F. D. Shields, "Sound absorption in the halogen gases," The Journal of the Acoustical Society of America **32**, 180–185 (1960), https://doi.org/10.1121/1.1908006.

[19]P. G. Dickens and A. Ripamonti, "Calculation of vibrational relaxation times in gases," Transactions of the Faraday Society **57**, 735–745 (1961), https://doi.org/10.1039/TF9615700735.

[20]F. I. Tanczos, "Calculation of vibrational relaxation times of the chloromethanes," The Journal of Chemical Physics **25**, 439–447 (1956), https://doi.org/10.1063/1.1742943.

[21]M. Camac, "O_2 vibration relaxation in oxygen-argon mixtures," The Journal of Chemical Physics **34**, 448–459 (1961), https://doi.org/10.1063/1.4757208.

[22]D. L. Matthews, "Vibrational relaxation of carbon monoxide in the shock tube," The Journal of Chemical Physics **34**, 639–642 (1961), https://doi.org/10.1063/1.1701000.

[23]J. Parker, "Effect of several light molecules on the vibrational relaxation time of oxygen," The Journal of Chemical Physics **34**, 1763–1772 (1961), https://doi.org/10.1063/1.1701075.

[24]E. W. Montroll and K. E. Shuler, "Studies in nonequilibrium rate processes. I. The relaxation of a system of harmonic oscillators," The Journal of Chemical Physics **26**, 454–464 (1957), https://doi.org/10.1063/1.1743326.

[25]R. Herman and K. E. Shuler, "Studies in nonequilibrium rate processes. IV. The rotational and vibrational relaxation of a system of rotating oscillators," The Journal of Chemical Physics **29**, 366–374 (1958), https://doi.org/10.1063/1.1744487.

[26]K. Takayanagi, "On the inelastic collision between molecules, II," Progress of Theoretical Physics **8**, 497–508 (1952), https://doi.org/10.1143/ptp/8.5.497.

[27]R. C. Millikan and D. R. White, "Systematics of vibrational relaxation," The Journal of Chemical Physics **39**, 3209–3213 (1963), https://doi.org/10.1063/1.1734182.

[28]J. P. Appleton, "Shock-tube study of the vibrational relaxation of nitrogen using vacuum-ultraviolet light absorption," The Journal of Chemical Physics **47**, 3231–3240 (1967), https://doi.org/10.1063/1.1712381.

[29]J. W. Rich and R. G. Rehm, "Population distributions during vibrational relaxation of diatomic gases," in *Symposium (International) on Combustion*, Vol. 11 (Elsevier, 1967) pp. 37–48, https://doi.org/10.1016/S0082-0784(67)80132-2.

[30]C. Park, "Assessment of a two-temperature kinetic model for dissociating and weakly ionizing nitrogen," Journal of Thermophysics and Heat Transfer **2**, 8–16 (1988), https://doi.org/10.2514/3.55.

[31]R. A. Allen, J. C. Comm, and J. C. Keck, "Radiation from hot nitrogen," Tech. Rep. (AVCO Everett Research Laboratory, Research report 102, 1961).

[32]R. A. Allen, J. C. Comm, and J. C. Keck, "Non-equilibrium radiation from shock heated nitrogen and a determination of the recombination rate," Tech. Rep. (AVCO Everett Research Laboratory, Research report 110, 1961).

[33]R. A. Allen, "Non-equilibrium shock front rotational, vibrational and electronic temperature measurements," Tech. Rep. (AVCO Everett Research Laboratory, Research note 459, 1964).

[34]L. Talbot, "Survey of the shock structure problem," American Rocket Society Journal **32**, 1009–1016 (1962), https://doi.org/10.2514/8.6193.

[35]B. Levitt and D. F. Hornig, "Structure of detonation waves in gases," The Journal of Chemical Physics **36**, 219–227 (1962), https://doi.org/10.1063/1.1732300.

[36]S. P. Sharma and W. Gillespie, "Nonequilibrium and equilibrium shock front radiation measurements," Journal of Thermophysics and Heat Transfer **5**, 257–265 (1991), https://doi.org/10.2514/3.259.

[37]M. Furudate, S. Nonaka, and K. Sawada, "Behavior of two-temperature model in intermediate hypersonic regime," Journal of Thermophysics and Heat transfer **13**, 424–430 (1999), https://doi.org/10.2514/2.6480.

[38]M. Furudate, S. Nonaka, and K. Sawada, "Calculation of shock shapes over simple geometry in intermediate hypersonic air flow," in *33rd Thermophysics Conference* (1999) p. 3686, https://doi.org/10.2514/6.1999-3686.

[39]M. Furudate and K. Sawada, "Effect of rotational nonequilibrium on shock standoff distances," in *39th Aerospace Sciences Meeting and Exhibit* (2001) p. 813, https://doi.org/10.2514/6.2001-813.

[40]K. Fujita, S. Sato, T. Abe, and Y. Ebinuma, "Experimental investigation of air radiation from behind a strong shock wave," Journal of Thermophysics and Heat Transfer **16**, 77–82 (2002), https://doi.org/10.2514/2.6654.

[41]J. G. Parker, "Rotational and vibrational relaxation in diatomic gases," The Physics of Fluids **2**, 449–462 (1959), https://doi.org/10.1063/1.1724417.

[42]C. Park, "Rotational relaxation of N_2 behind a strong shock wave," Journal of Thermophysics and Heat Transfer **18**, 527–533 (2004), https://doi.org/10.2514/1.11442.

[43]L. Rahn and R. E. Palmer, "Studies of nitrogen self-broadening at high temperature with inverse raman spectroscopy," Journal of the Optical Society of America B **3**, 1164–1169 (1986), https://doi.org/10.1364/JOSAB.3.001164.

[44]C. Park, "The limits of two-temperature kinetic model in air," in *48th AIAA Aerospace Sciences Meeting Including the New Horizons Forum and Aerospace Exposition* (2010) p. 911, https://doi.org/10.2514/6.2010-911.

[45]I. D. Boyd and E. Josyula, "State resolved vibrational relaxation modeling for strongly nonequilibrium flows," Physics of Fluids **23**, 057101 (2011), https://doi.org/10.1063/1.3584128.

[46]J. G. Kim, O. J. Kwon, and C. Park, "Master equation study and nonequilibrium chemical reactions for H+ H_2 and He+ H_2," Journal of Thermophysics and Heat Transfer **23**, 443–453 (2009), https://doi.org/10.2514/1.41741.

[47]J. G. Kim, O. J. Kwon, and C. Park, "Master equation study and nonequilibrium chemical reactions for hydrogen molecule," Journal of Thermophysics and Heat Transfer **24**, 281–290 (2010), https://doi.org/10.2514/1.45283.

[48]J. G. Kim and I. D. Boyd, "State-resolved thermochemical nonequilibrium analysis of hydrogen mixture flows," Physics of Fluids **24**, 086102 (2012), https://doi.org/10.1063/1.4747340.

[49]J. G. Kim and I. D. Boyd, "Master equation analysis of post normal shock waves of nitrogen," Journal of Thermophysics and Heat Transfer **29**, 241–252 (2015), https://doi.org/10.2514/1.T4249.

[50]C. Kim, K. H. Kim, Y. Yang, and J. G. Kim, "Effect of multi-temperature models on heat transfer and electron behavior in hypersonic flows," Physics of Fluids **36**, 096127 (2024), https://doi.org/10.1063/5.0223900.

[51]R. S. Myong, "Thermodynamically consistent hydrodynamic computational models for high-Knudsen-number gas flows," Physics of Fluids **11**, 2788–2802 (1999), https://doi.org/10.1063/1.870137.

[52]B. C. Eu, *Kinetic Theory and Irreversible Thermodynamics* (Wiley-Interscience, 1992) p. 752.

[53]T. K. Mankodi and R. S. Myong, "Boltzmann-based second-order constitutive models of diatomic and polyatomic gases including the vibrational mode," Physics of Fluids **32**, 126109 (2020), https://doi.org/10.1063/5.0026687.

[54]D. A. Andrienko and I. D. Boyd, "High fidelity modeling of thermal relaxation and dissociation of oxygen," Physics of Fluids **27**, 116101 (2015), https://doi.org/10.1063/1.4935241.

[55]P. V. Marrone and C. E. Treanor, "Chemical relaxation with preferential dissociation from excited vibrational levels," Physics of Fluids **6**, 1215–1221 (1963), https://doi.org/10.1063/1.1706888.

[56]H. Srivastava, T. K. Mankodi, and R. S. Myong, "Second-order constitutive relations and their topologies for rotational non-equilibrium in diatomic gas flows using a multi-temperature approach," Physics of Fluids **37**, 036154 (2025), https://doi.org/10.1063/5.0259816.

[57]S. Zeng, Z. Yuan, W. Zhao, and W. Chen, "Numerical simulation of hypersonic thermochemical nonequilibrium flows using nonlinear coupled constitutive relations," Chinese Journal of Aeronautics **36**, 63–79 (2023), https://doi.org/10.1016/j.cja.2022.09.013.

[58]R. N. Gupta, J. M. Yos, R. A. Thompson, and K. P. Lee, "A review of reaction rates and thermodynamic and transport properties for an 11-species air model for chemical and thermal nonequilibrium calculations to 30000 K," Tech. Rep. (NASA, Report No. NASA-RP-1232, 1990) https://www.osti.gov/servlets/purl/4420349.

[59]S. Zeng, J. Yang, W. Zhao, Z. Yuan, G. Fan, and W. Chen, "Nonlinear coupled constitutive relations for hypersonic reacting flows with thermal nonequilibrium effect," Physics of Fluids **37**, 016116 (2025), https://doi.org/10.1063/5.0249391.

[60]G. Garg, T. K. Mankodi, E. Esmaeilifar, and R. S. Myong, "Neural network-based finite volume method and direct simulation Monte Carlo solutions of non-equilibrium shock flow guided by nonlinear coupled constitutive relations," Physics of Fluids **36**, 106113 (2024), https://doi.org/10.1063/5.0223654.

[61]G. Garg, T. K. Mankodi, and R. S. Myong, "Fast neural network-based direct simulation Monte Carlo solutions of shock flow of diatomic gases with vibrational modes," Physics of Fluids **37**, 076105 (2025), https://doi.org/10.1063/5.0265564.

[62]J. A. Lordi and R. E. Mates, "Rotational relaxation in nonpolar diatomic gases," The Physics of Fluids **13**, 291–308 (1970), https://doi.org/10.1063/1.1692920.

[63]P. Valentini, C. Zhang, and T. E. Schwartzentruber, "Molecular dynamics simulation of rotational relaxation in nitrogen: Implications for rotational collision number models," Physics of Fluids **24**, 106101 (2012), https://doi.org/10.1063/1.4757119.

[64]S. M. Jo, M. Panesi, and J. G. Kim, "Prediction of shock standoff distance with modified rotational relaxation time of air mixture," Physics of Fluids **33**, 047102 (2021), https://doi.org/10.1063/5.0045842.

[65]A. Yakunchikov, V. Kosyanchuk, and A. Iuldasheva, "Rotational relaxation model for nitrogen and its application in free jet expansion problem," Physics of Fluids **32**, 102006 (2020), https://doi.org/10.1063/5.0021704.

[66]C. A. Brau and R. M. Jonkman, "Classical theory of rotational relaxation in diatomic gases," The Journal of Chemical Physics **52**, 477–484 (1970), https://doi.org/10.1063/1.1673010.

[67]C. Park, "Problems of rate chemistry in the flight regimes of aeroassisted orbital transfer vehicles," in *19th Thermophysics Conference*, Vol. 96 (AIAA, 1984) pp. 511–537, https://doi.org/10.2514/6.1984-1730.

[68]R. S. Myong, "A generalized hydrodynamic computational model for rarefied and microscale diatomic gas flows," Journal of Computational Physics **195**, 655–676 (2004),

https://doi.org/10.1016/j.jcp.2003.10.015.

[69]R. S. Myong, "On the high Mach number shock structure singularity caused by overreach of Maxwellian molecules," Physics of Fluids **26**, 056102 (2014), https://doi.org/10.1063/1.4875587.

[70]M. Al-Ghoul and B. C. Eu, "Generalized hydrodynamics and shock waves," Physical Review E **56**, 2981–2992 (1997), https://doi.org/10.1103/PhysRevE.56.2981.

[71]T. K. Mankodi, O. Ejtehadi, T. Chourushi, A. Rahimi, and R. S. Myong, "nccrFOAM suite: Nonlinear coupled constitutive relation solver in the OpenFOAM framework for rarefied and microscale gas flows with vibrational non-equilibrium," Computer Physics Communications **296**, 109024 (2024), https://doi.org/10.1016/j.cpc.2023.109024.

[72]Singh, S. and Karchani, A. and Sharma, K. and Myong, R. S., "Topology of the second-order constitutive model based on the Boltzmann–Curtiss kinetic equation for diatomic and polyatomic gases," Physics of Fluids **32**, 026104 (2020), https://doi.org/10.1063/1.5133079.

[73]G. Garg, T. K. Mankodi, and R. S. Myong, "Topology of direct simulation Monte Carlo constitutive relations for neural network-accelerated finite-volume solutions of velocity-shear flows," Physics of Fluids **38**, 036125 (2026), https://doi.org/10.1063/5.0316610.

[74]J. D. Anderson, *Modern Compressible Flow: With Historical Perspective, 4th Edition* (McGraw Hill, Inc., 1995) p. 792.

[75]W. Zhang, Z. Zhang, X. Wang, and T. Su, "A review of the mathematical modeling of equilibrium and nonequilibrium hypersonic flows," Advances in Aerodynamics **4**, 1–47 (2022), https://doi.org/10.1186/s42774-022-00125-x.

[76]W. G. Vincenti and C. H. Kruger, *Introduction to Physical Gas Dynamics* (Krieger Pub. Co.; Reprint edition, 1975) p. 556.

[77]E. F. Toro, *Riemann Solvers and Numerical Methods for Fluid Dynamics: A Practical Introduction* (Springer-Verlag Berlin and Heidelberg GmbH & Co. K; 3rd ed., 2009) p. 724.

[78]H. Alsmeyer, "Density profiles in argon and nitrogen shock waves measured by the absorption of an electron beam," Journal of Fluid Mechanics **74**, 497–513 (1976), https://doi.org/10.1017/S0022112076001912.

[79]R. Miles, A. Dogariu, and L. Dogariu, "Localized time accurate sampling of nonequilibrium and unsteady hypersonic flows: methods and horizons," Experiments in Fluids **62**, 248 (2021), https://doi.org/10.1007/s00348-021-03332-2.

[80]G. A. Bird, *Molecular Gas Dynamics and the Direct Simulation of Gas Flows* (Oxford University Press, Oxford, 1994) p. 476.

[81]T. K. Mankodi, U. V. Bhandarkar, B. P. Puranik, "Hypersonic flow over Stardust Re-entry Capsule using ab-initio based chemical reaction model," Acta Astronautica **162**, 243–255 (2019), https://doi.org/10.1016/j.actaastro.2019.06.021.

[82]Z. Yuan, Z. Jiang, W. Zhao, and W. Chen, "Multiple temperature model of nonlinear coupled constitutive relations for hypersonic diatomic gas flows," AIP Advances **10**, 055023 (2020), https://doi.org/10.1063/5.0010232.